

# **Anisotropy of Land Surface Skin Temperature Derived from Satellite Data**

Patrick Minnis

Atmospheric Sciences Research

NASA Langley Research Center

Hampton, Virginia

Mandana M. Khaiyer

Analytical Services and Materials, Inc.

Hampton, Virginia

Revision for *Journal of Applied Meteorology*

June 1999

## **Abstract**

The land skin temperature, an important feature for agricultural monitoring, convective processes, and the Earth's radiation budget, is monitored from limited-view satellite imagers. The angular dependence of this parameter is examined using simultaneous views of clear areas from up to three geostationary satellites. Daytime temperatures from different satellites differed by up to 6K and varied as a function of the time of day. Larger differences are expected to occur, but were not measured because of limited viewing angles. These differences suggest that biases may occur in both the magnitude and phase of the diurnal cycle of skin temperature and its mean value whenever geostationary satellite data are used to determine skin temperature. The temperature differences were found over both flat and mountainous regions with some slight dependence on vegetation. The timing and magnitude of the temperature differences provide some initial validation for relatively complex model calculations of skin temperature variability. The temperature differences are strongly correlated with terrain and the anisotropy of reflected solar radiation for typical land surfaces. These strong dependencies suggest the possibility for the development of a simple empirical approach for characterizing the temperature anisotropy. Additional research using a much greater range of viewing angles is required to confirm the potential of the suggested empirical approach.

## Introduction

Surface skin temperature and its temporal variation are critical parameters for determining the longwave radiative flux leaving the surface and, in many cases, the top of the atmosphere. They are also used in the diagnosis of plant condition, frost occurrence, and soil moisture and in the determination of cloud optical properties. The skin temperature can be computed from physical models or determined via remote sensing of infrared radiation. In the latter case, the observed radiance must be corrected for the surface emissivity and any attenuation by the atmosphere between the surface and sensor. For water bodies, the remotely sensed skin temperature is some integral of the temperature in the uppermost layers of the water and is relatively straightforward to understand. The skin temperature of land surfaces is considerably more complex because vegetation, topography, soil inhomogeneities, and small-scale roughness comprise the surface.

Land surface temperatures generally respond rapidly to changes in solar illumination so that the remotely sensed temperature depends on the viewing perspective. For example, the nadir view of a forest canopy may see some of the underlying ground while a more oblique view may see only foliage and bark. If the ground is shadowed, it will probably be cooler than the illuminated canopy. Similarly, the poleward side of a mountain beyond the Tropics is often in shadow while the equatorward face is in sunshine for much of a given day depending on the season and terrain roughness. The latter side will warm more than the former. Even at night, the morphology of a vegetation canopy or rock formation may also induce some anisotropy because of differential cooling rates between the lower-level surfaces that have limited exposure to the sky and the upper-level surfaces that are more exposed and may also be more thoroughly ventilated. The outgoing longwave flux from a given region is the integral of the radiation leaving the area from all angles. Thus, to accurately compute the flux from a skin temperature derived from a radiance measured from a single angle, it is necessary to understand and account for any such viewing angle anisotropy.

The anisotropy of shortwave radiation reflected from the Earth's surface has long been accepted and taken into account for many satellite-remote sensing applications (e.g., Minnis and Harrison 1984, Suttles et al. 1988). Although it is known that longwave radiation observed at the top

of the atmosphere varies with viewing zenith angle (VZA) due to the limb darkening effects of the atmosphere (e.g., Minnis et al., 1984), it is typically assumed that the surface-emitted radiation does not vary substantially with angle for a given surface type (e.g., Rossow and Garder, 1993). The VZA dependence of surface emissivity, however, is recognized and has been measured for a few surfaces. Several studies have documented that measured infrared brightness temperatures of a given scene can vary for several reasons. For example, infrared brightness temperatures measured from a detector 2 m above the surface varied by up to 8 K depending on surface type and VZA (Lagourde and Kerr 1993). Various theoretical models have been developed to account for some of these differences (e.g., Sobrino and Casselles 1990). Other modeling studies have demonstrated that an azimuthal variation in temperature should occur due to canopy structure (McGuire et al. 1988) and extreme terrain morphology (Lipton and Ward 1997). Canopy temperature variations that are dependent on both VZA and relative azimuth angle (RAZ) have been measured on a small scale (McGuire et al. 1988). Wong et al. (1996) used helicopter data as well as coincident Geostationary Operational Environmental Satellite (GOES) data to illustrate the magnitude of the temperature differences on a large scale for several surface types. Variations as large as 5 K over a forested mountain region were detected using multi-angle view satellite data. The dependence of brightness temperature on RAZ, VZA, solar zenith angle (SZA), topography, and vegetation cover, however, has not been adequately determined from observations or characterized in models. From a remote sensing perspective, a relatively simple approach to account for these dependencies is desirable. Using simultaneous multiple satellite views, this paper further explores the anisotropy of clear-sky brightness temperature, its potential effect on the outgoing longwave radiation (OLR), and the parameters that may be useful for modeling the anisotropy.

Surface skin temperature is defined here as the equivalent blackbody temperature of the solid and/or liquid surfaces that radiate directly to space through the atmosphere. The surface that radiates in a given direction from a particular location will, in general, be different from the surface radiating to space at any other direction because of the three-dimensional nature of land surfaces. No attempt is made here to distinguish between different surfaces such as the canopy and the ground or the grass and

the soil. Rather, the radiating temperature of various, unknown combinations of these surfaces is the focus of this study.

## **Data and Methodology**

GOES-8, 9, and 10 4-km-resolution channel-4 (infrared window, IR; 10.8  $\mu\text{m}$ ) imager datasets were obtained from the University of Wisconsin Space Science and Engineering Center McIDAS archive for various cloud-free days during 1998. The satellites were spaced between 75°W and 135°W longitude during early 1998 as shown in Fig. 1. GOES-10 was located at ~105°W midway between GOES-9 and GOES-8. To ensure proper alignment, small navigational adjustments were interactively determined and applied to either a GOES-9 or GOES-10 image to match the corresponding GOES-8 image. The precision of the navigation between images is approximately 2-3 km. The IR data from each satellite were sectioned into the 1° x 1° or 2° x 2° regions that are indicated with a letter in Fig. 1. These regions were selected to sample a variety of terrain features, vegetation types, and viewing perspective differences. Cloud-free days were determined through visual inspection of the visible (channel-1) and IR images and image loops, as well as the images of the brightness temperature differences between channels 2 and 4 and between channels 4 and 5. Within each region, the data were further subdivided into 10' sub-boxes to assign an International Geosphere Biosphere Programme (IGBP) vegetation type (Belward and Loveland 1996, see [http://tanalo.larc.nasa.gov:8080/surf\\_htmls/sce\\_type](http://tanalo.larc.nasa.gov:8080/surf_htmls/sce_type)). Generalized categories of vegetation type were defined by grouping similar IGBP types. For example, combined crop/grassland includes grassland, cropland, and mixed grass-forest IGBP types. The average IR radiance was calculated and converted to a mean equivalent blackbody temperature  $T$  at a given time for each selected 10' box, SZA, and vegetation type. An average of all 10' boxes with the same vegetation type was then calculated to represent the region. This process resulted in a relatively large number of pixels for each vegetation type in a region. For example, a 1° x 1° region in the central United States contains roughly 500 pixels. If three distinct vegetation types cover the region equally, then the mean brightness temperatures for a given vegetation type in that region would be computed from almost 170 pixels.

Additionally, only vegetation types covering at least 10% of a  $2^\circ \times 2^\circ$  region were used. Any differences in the matched temperatures due to navigation and parallax errors due to terrain height are negligible for samples of this size.

All of the channel-4 calibrations were provided as part of the McIDAS dataset. To account for any calibration differences between the satellites, the IR temperatures from G9 and G10 were adjusted to the calibration of G8. Normalization formulae were derived by matching the pixels centered on the longitude midway between the two satellite longitudes at local noon and late at night (midnight to sunrise) over both land and water. Data from  $16^\circ\text{N}$  to  $46^\circ\text{N}$  and from  $22^\circ\text{N}$  to  $47^\circ\text{N}$  were used for G9 and G10, respectively. The temperatures of the matched pixels were averaged in equivalent radiances and converted back to equivalent blackbody temperatures. Least squares linear regression was performed to obtain the G9 and G10 normalization equations. Figures 2a and 2b show the scatterplots and regression fits for G9 and G10, respectively, for the nighttime data. The resulting fits for the data in Fig. 2 are

$$T(G9) = 0.9992 T'(G9) + 0.5664, \quad (1)$$

and

$$T(G10) = 1.0043 T'(G10) - 0.7643. \quad (2)$$

where  $T'$  is the observed value and  $T$  is the value normalized to G8 temperatures that serves as the observed value for the other satellites. Although the squared linear correlation coefficients  $R^2$  for G9 and G10 are 0.992 and 0.998, respectively, the G9 data appear to be much noisier than the G10 temperatures. To determine the uncertainty in the fit, both datasets were regressed using reversed independent variables. The rms differences in the predicted values for the two fits are 0.10K and 0.03K for G9 and G10, respectively. The daytime fit for G10 was almost identical to (2) with a rms difference in predicted values of 0.09K. However, the G9 daytime fit yields temperatures that are

biased by  $\sim 1.0\text{K}$  relative to those computed with (1). The reasons for the day-night difference are most likely due to differential heating of the surfaces observed from the two satellites, the phenomenon that is being studied here. Most of the land regions observed at  $105^\circ\text{W}$  contain mountains where the differential heating is greatest (see below), while those at  $90^\circ\text{W}$  are primarily flat lands. To minimize such effects, only (1) and (2) were used to adjust all of the observed G9 and G10 temperatures, respectively, before further processing. Based on the comparisons between the reverse fits and the G8-G10 day-night comparison, it is estimated that the uncertainty in the normalization is  $\pm 0.10\text{K}$  and  $\pm 0.30\text{K}$  for G10 and G9, respectively. The latter value was determined by increasing the G8-G9 reverse fit difference by a factor of 3, the day-night fit difference factor found for the G8-G10 comparison.

An additional correction was applied to the G9 data because of persistent shifts in the G8 and G9 temperature difference time series over all regions at particular hours. The hours with shifts were determined by examining the difference time series and the G9 temperature time series over clear water pixels. The corrections,  $-0.65$  and  $0.28\text{K}$ , are added to  $T(\text{G9})$  observed at 2 hours only, 0715 and 1015 UTC, respectively, for all days during April 1998. Similar shifts were not seen in the differences between the G8 and G10 temperatures. The source of the shifts is not known, but the corrections are relatively small and serve only to smooth the observed nocturnal difference plots.

The effect of the intervening atmosphere on the observed temperatures  $T_{obs}$  was removed with a radiative transfer model that accounts for the absorption and emission in each atmospheric layer. In discrete form, the observed radiance is

$$B(T_{obs}) = \sum_{i=0}^n B(T_i)(1 - \epsilon_{i+1}) + \epsilon_{i+1}B(T_{i+1}), \quad (3)$$

where the skin temperature  $T_s = T_0$  and the emissivity of atmospheric layer  $i$ ,  $\epsilon_i$  is determined by the absorption optical depth and VZA. The correlated- $k$  distribution approach (Kratz 1995) was used to determine the optical depth of each layer using the temperature and humidity profile from the closest 3-hourly, 60-km resolution Rapid Update Cycle analyses (Benjamin et al. 1994) for April data and the nearest radiosonde measurements for the May data. This correction yields the apparent surface skin

temperature  $T_s(Gx)$ , where  $Gx$  is the satellite indicator and  $x$  is the satellite number. This quantity, designated “apparent” because it has not been corrected for surface emissivity, is the only temperature discussed hereafter unless otherwise noted. For simplicity, skin or surface temperature is assumed to be equivalent to apparent skin temperature. The corrections varied with atmospheric humidity and VZA. The average difference between  $T_{obs}$  and  $T_s$  was  $\sim 1.1\text{K}$ . The largest difference was  $3.8\text{K}$  for a few hours of G9 data over region E. The smallest correction was  $0.3\text{K}$  for a few hours of G10 data over region M.

The radiative transfer model of Fu and Liou (1993) was used to compute  $OLR(Gx)$  based on the retrieved values of  $T_s$  and a representative temperature and humidity profile for each separate region. Because the OLR is the broadband longwave ( $5 - 50 \mu\text{m}$ ) flux, it includes radiances emitted by the surface and atmosphere over all angles and relevant wavelengths in contrast to the IR radiance observed at one angle.

The apparent skin temperature difference,

$$BTD_x = T_s(G8) - T_s(Gx), \quad (4)$$

between two of the GOES satellites constitutes a measure of anisotropy. Land bidirectional reflectance distribution functions (BRDF) for the GOES visible channel were taken from the model of Minnis and Harrison (1984) as a measure of the solar reflectance anisotropy. These models are designated by the variable  $(SZA, VZA, RAZ)$ . The topography for each region was characterized by its mean altitude  $Z$  and the standard deviation of altitude  $\sigma_z$  within the region. Values for these parameters were derived from the 10' elevation maps of the U.S. Navy (available from U.S. Geological Survey at <http://grid2.cr.usgs.gov/data/navy.10min.elev.html>). The mean elevation is given to the nearest 30 m. Table 1 lists the characteristics of the regions used in this study.

## Results



GOES-8, 9, and 10 surface temperatures taken during 3 April 1998 for region A, a relatively flat grassland (Table 1), reveal differences in their diurnal cycles (Fig. 3), even though two of the satellites viewed the area from almost the same VZA. The temperatures agreed to within 0.3K during most of the night and diverged after sunrise (Fig. 4). The maxima for all three satellites occurred within 0.5 h of 1300 LT (Local Time) although the maximum temperature for G9 was greater than that for the other two satellites. In general, the temperature from the satellite east of a region's longitude was higher during the morning and lower during the afternoon relative to the more westerly satellite. Figure 4 shows the time series of both  $BT D_9$  and  $BT D_{10}$ . The latter ranges from 0.7K to almost -2.0K, while the former reaches almost 2.5K before dropping to -2.5K near mid-afternoon. Both  $BT D_9$  and  $BT D_{10}$  reach relatively steady values of -0.3K at night. The difference at night may be due to several factors such as VZA-dependent surface emissivity in the case of  $BT D_{10}$  or to calibration errors in the case of  $BT D_9$ .

Region B, approximately 150 km northwest of A, consists of forested mountains and rolling shrub and grasslands. For the flatland (including crop/grassland) parts of B,  $BT D_{10}$  reaches a slightly larger value (1.0 to 1.5K) than in region A, but for the forested parts of B,  $BT D_{10}$  attains a value more than twice that for the grasslands comprising region A (Fig. 5a). The peak values occur at about the same time for both regions A and B. Minimum values of  $BT D_{10}$ , between -2.0 and -3.5K, occur near local noon for region B instead of mid-afternoon for region A because of the close proximity of G8 to G10. The relative differences between regions B and A are similar for  $BT D_9$  (Fig. 5b). The maxima, around 1030 LT, reached almost 4K for the forested boxes. The minima, ~ -4K, were lower than those in region A but occur at about the same time. Both  $BT D_9$  and  $BT D_{10}$  essentially follow the same diurnal patterns on both days.

To ensure that these differences are not due to some spurious diurnal cycles in the GOES IR channels,  $BT D_9$  and  $BT D_{10}$  were computed using temperatures taken during 2 days over open water in region C (see Fig. 1). From the lower curves in Fig. 6, it is seen that  $BT D_9$  varies by 0.2K over the day with a mean value of -0.62K.  $BT D_{10}$  varies by 0.3K with a mean of -0.68K. While these results suggest that the calibrations are biased, they are based on skin temperatures derived from different

VZAs. To account for the VZA effect, the skin temperatures were adjusted by dividing the equivalent radiance by the surface emissivity at  $10.8\ \mu\text{m}$  at the VZA of the satellite (see Table 1) and then computing the temperatures. The emissivities were taken from the  $11\text{-}\mu\text{m}$  sea water model of Masuda et al. (1988) using a wind speed of  $5\text{ms}^{-1}$ . The *BTDS* computed from these emissivity-corrected temperatures (upper curves in Fig. 6) vary by the same amounts as before, but the mean differences are  $-0.10\text{K}$  and  $-0.02\text{K}$  for G9 and G10, respectively. These differences show that the normalization errors are negligible. The variations in *BTD* over water are also minimal as would be expected from the mixing in the upper layer of the sea and the lack of a solid structure that could produce persistent shading.

Over the adjacent coastland, between regions K and D,  $BT_{D_9}$  and  $BT_{D_{10}}$  reach 4 and 2K, respectively. These differences were negligibly affected by navigation errors because of the large number of pixels (between 100 and 600) used to compute the averages for each vegetation type in these two regions. Thus, it is clear that the observed brightness temperatures over land differ primarily because of differences in the temperatures of the respective land structures observed by a given satellite. Further north in region D, the large diurnal cycles in  $T_s(Gx)$  were slightly out of phase with a  $\sim 1\text{-h}$  range in the time of maximum temperature (Fig. 7a). The *BTDS* over the mountainous deciduous forest part of this region are also quite substantial ranging from 1.5 to  $-3\text{K}$  for  $BT_{D_{10}}$  (Fig. 7b) and from 2.8 to  $-3.5\text{K}$   $BT_{D_9}$  (Fig. 7c). The *BTD* diurnal range is smaller for the open shrubland in this same region. In regions C and D, the VZA for G9 was less than that for G8.

The VZA for G8 was less than that for G9 in E, a relatively flat region in Texas covered with farms and forest. Here, the diurnal range in  $BT_{D_{10}}$  is only 2K (Fig. 8a), compared to 3K for  $BT_{D_9}$  (Fig. 8b), and is entirely positive during the morning for both satellite pairs. No significant difference is evident between the forested and cropland areas. Further to the north and east, over region F, (Fig. 9), the differences in VZA between G9 and G8 were greater and the range in  $BT_{D_9}$  is as large as 3K for the crop/mosaic areas compared.  $BT_{D_{10}}$  varies by only 1K. At more extreme VZAs, the *BTDS* are still significant. Figure 10 shows  $BT_{D_9}$  for two regions, G and H, viewed by G8 at  $68^\circ$  and  $74^\circ$ , respectively, compared to  $63^\circ$  and  $68^\circ$  by G9. The average difference between  $RAZ(G8)$  and

RAZ(G9) for these two regions is roughly  $55^\circ$ , the smallest differences for any of the considered regions. Over the diurnal cycle,  $BT D_9$  ranges by 3 and 2K over G and H, respectively. The differences are negative during the afternoon and slightly positive during the short night and early morning for region G.  $BT D_9$  slowly approaches zero at night over region H and begin to decrease shortly after sunrise.

Figure 11 shows an extremely large range in both  $BT D_9$  and  $BT D_{10}$ , for region I in the mountains of northwestern Mexico.  $BT D_{10}$  varies from 3K to  $-3$ K for the forested areas and less for the grassland and crop parts of the region (Fig. 11a). The maximum value of  $BT D_9$  is 5.6K, while the minimum drops to  $-5$ K for the forested areas (Fig. 11b). Similar to  $BT D_{10}$ , an even larger range,  $\sim 12$ K, is found if the evergreen forests are considered separately. The less vegetated areas have a much smaller BT D range. The VZAs for G8 and G9 differed by only  $5^\circ$ . Other regions in the same area (J, K, L, and M) also show substantial diurnal ranges in BT D.

To illustrate the potential impact of these BT D variations on clear-sky longwave flux, the OLR was computed for time series of  $T_s$  from G8 and G9 for selected vegetation types within regions A, B, and I. Figure 12 shows that the two satellites yield a range of daytime OLR differences from 14 to  $-13$   $\text{Wm}^{-2}$  in OLR for region I (Fig. 12). The mean daytime OLR(G8-G9) differences and their standard deviations for region I are  $1.5 \pm 9.5$   $\text{Wm}^{-2}$ . Over the flatter terrain of region A, the daytime OLR differences vary from 4 to  $-6$   $\text{Wm}^{-2}$  with a mean and standard deviation of 0.3 and 3.4  $\text{Wm}^{-2}$ . The difference range is 14  $\text{Wm}^{-2}$  for region B with a mean and standard deviation 0.4 and 4.5  $\text{Wm}^{-2}$ . At night, the OLR differences vary from  $-1$  to  $-4$   $\text{Wm}^{-2}$ . The standard deviations of the daytime G10 OLR differences are smaller than those for G9, but the magnitudes of the means are larger,  $-1.7$ ,  $-1.6$ , and  $-12.4$   $\text{Wm}^{-2}$  for regions A, B, and I, respectively.

## Discussion

The magnitude of the temperature differences arising from viewing perspective suggest that the anisotropy in longwave radiance should be taken into account when deriving land surface skin temperature or clear-sky OLR from satellite-observed radiances. Any validation exercises involving

the comparison of satellite-observed infrared radiances with model predictions of the same quantity should also allow for uncertainties arising from this anisotropy. While the differences averaged over the entire day may not be particularly significant, the surface-emission anisotropy can have a substantial impact on the interpretation of the radiance field. For example, if OLR were computed from each of the derived values of  $T_s(Gx)$  in Fig. 7a, for example, the phase of the diurnal cycle in OLR would vary as a function of the geostationary satellite viewing geometry because it would follow the variation of  $T_s$  very closely. The phase of the diurnal cycle in surface heating impacts the micrometeorology of the surface layer and the onset of convective processes. The three views in Fig. 7a yielded a ~1-hour range in the phase of the diurnal cycle for  $T_s(Gx)$  in the observed area. Other viewing combinations may have produced a wider range.

Monitoring of surface and agricultural conditions using geostationary satellite data may not be affected much by temperature anisotropy if the procedure relies on relative day-to-day changes at a given hour. However, if the monitoring relies on a Sun-synchronous satellite that views from a different angle each day or on the magnitude of the temperature rather than on relative changes in temperature, this anisotropy could be mistaken for actual changes in the skin temperature. Given the results in Fig. 12, it is clear that the OLR derived from geostationary satellites will be biased at a given local time, and perhaps on average, if the anisotropy is ignored. Similarly, satellites in mid-inclined orbits such as the Earth Radiation Budget Satellite or the Tropical Rainfall Measuring Mission (TRMM) satellite will have extremely limited views of regions near the latitude of their orbital inclination if they measure infrared radiances with a cross-track scanning instrument. Near its maximum latitude, this type of satellite always views towards the Tropics for regions at lower latitudes and poleward for regions at higher latitudes. For these regions, biases arising from skin brightness temperature anisotropy are unlikely to average out over the course of a month. To develop methods for taking this anisotropy into account, it is necessary to examine the factors governing its variation.

In addition to the lack of daytime variability over water, the nightly return of BTD to near-zero values for all of these cases clearly shows that the differences are solar-driven. The anisotropy of  $T_s$  is forced by a variety of factors such as shadowing, surface heat capacity, and surface emissivity. The

portion of scene receiving the most sunlight will warm fastest, while the most shaded portion should remain the coolest. In most cases, the BTD does not return exactly to zero or a constant value immediately when the sun sets. Rather, the BTD appears to approach zero very rapidly before sunset then gradually approaches a constant value (e.g., Fig. 7c) or immediately reaches the constant value just after sunset (e.g., Fig. 8a). Sometimes, the part of the scene that receives the greater portion of sunlight during the afternoon apparently requires more time to cool than the more shadowed part. This shadowed area cools during the afternoon relative to the sunlit side so it begins approaching a temperature independent of viewing angle before the sun sets. A quantitative description of the skin temperature's approach to a nocturnal value invariant with view will depend on many factors including scene morphology, soil and boundary-layer moisture, and wind speed and direction. Furthermore, the surface emissivity may have a VZA dependence that would yield a lower temperature for the satellite with the larger VZA. Figure 6 demonstrates this effect quite clearly. The reasons for the nocturnal BTDs are complex, but will not be considered further here because nighttime BTDs are minor relative to those observed during the day.

The anisotropy of reflected solar radiation over land provides one relative measure of illumination for a particular set of angles. For example, the maximum reflectance generally occurs at the antisolar point, while the minimum reflectance occurs in the forward scattering hemisphere where shadowing is usually greatest (e.g., Kriebel, 1978). Figure 13 shows the time series of  $BTD_g$  and the anisotropic reflectance factors for G8 and G9,  $\rho_g$  and  $\rho_g$ , respectively, for region B. As the two anisotropic factors diverge,  $BTD_g$  increases. As  $BTD_g$  switches sign,  $\rho_g$  becomes greater than  $\rho_g$  and diverges again. Scatterplots of mean  $BTD_g$  and the corresponding BRDF differences,  $\rho_g = \rho_g - \rho_g$ , between G8 and G9 (Fig. 14) show a strong correlation ( $R^2 = 0.96$ ). A least squares regression fit to

$$BTD_x = a_x \rho_x + b_x, \quad (5)$$

where the subscript  $x$  is the satellite indicator,  $a$  is the slope and  $b$  is the offset, yields  $a_g = 8.8$  and  $b_g = 0.07$  for the forested area of region B (Fig. 13). The data for  $BTD_{10}$  and  $\rho_{10}$  are also highly

correlated ( $R^2 = 0.86$ ) but line up along a different slope ( $a_9 = 10.6$ , not shown). The azimuth difference between G8 and G10 is less than that between G8 and G9, while differences in the VZAs are comparable. The correlations indicate that the BRDF differences, on average, account for more than 90% of the variance for  $BT D_9$  and  $BT D_{10}$ . The correlations for the data from regions A and I in Fig. 14 are also very substantial with  $R^2$  equal to 0.96 and 0.92, respectively. Region I has the greatest slope (12.6), while region A has the smallest (5.0) of the three areas in Fig. 14. The level of correlation is similar for nearly all of the other regions represented in Table 1 with  $R^2$  ranging from 0.86 to 0.98. For  $BT D_{10}$  from region F,  $R^2$  equals 0.77, while for  $BT D_9$  from region H,  $R^2$  is only 0.34. In those areas, the slope is very small. Nevertheless, the correlations are significant in all cases.

Vegetation clearly induces some anisotropy as seen in Fig. 8 for flat region E near Houston, Texas and in the measurements of McGuire et al. (1989). The grass, shrub, or canopy structure can induce some shadowing that will produce  $T_s$  anisotropy, but on a larger scale, it is clear from Fig. 14 that the undulations in the terrain can be much more important. For example, one satellite may view more of the valleys than another so it will see large shaded areas during part of the day while the other satellite may only see a fraction of the valleys. The difference in temperature between a sunlit mountainside and a valley that is still shaded after several hours of sunshine should be much larger than that between a sunlit tree and the shadowed ground behind it. Lipton and Ward's (1997) theoretical study predicted that the rugged terrain of the Colorado Rockies would produce substantial biases (up to 9°C) relative to the true surface temperature and apparent shifts in the phase of the  $T_s$  diurnal cycle, depending on the particular satellite view. Their study also demonstrated that the BT D between geostationary satellites at 86°W and 135°W would reach a maximum of ~6°C during the late morning and shift signs at noon over the Sierra Nevada range (~36°N, 112°W). The relative viewing conditions and terrain are similar to those corresponding to the results in Fig. 5b, which shows that the maximum  $BT D_9$  of 4°C consistently occurs near 1000 LT.  $BT D_9$  passes through zero approximately 1 hour before local noon. Although the conditions are not identical, such results tend to confirm the detailed theoretical model calculations. The Lipton and Ward (1997) model also predicts that the BT D

increases with a rise in the average slope of the terrain. The larger ranges in BTD for the mountainous regions observed here produce regression slopes that are larger than those for the flatter lands.

To better quantify the dependence on terrain, the slopes resulting from the linear regressions on (5) were further regressed against  $\alpha_z$ , a parameter that describes the ruggedness of the region. Figure 15 shows the scatterplots of  $\alpha_x$  versus  $\alpha_z$  and the resulting regression fit lines for  $\alpha_x$  versus  $\alpha_z$ . Each data point for a given value of  $\alpha_z$  represents a different vegetation type within each specific region. Each scene type must occupy more than 10% of the region to be included in this plot. In both cases, the large-scale morphology has a significant effect on the  $T_s$  anisotropy. The correlations ( $R^2 = 0.58$  and  $0.64$  for G8-G9 and G8-G10, respectively) here are relatively tight considering the differences in VZA ( $\sim 18^\circ$ ) and solar illumination for the various regions contributing to the dataset. In this dataset, the same value of  $\alpha_z$  is used for each vegetation type within a region. Thus, differences in terrain within a region that are related to vegetation type are not taken into account. For example, grasslands or croplands that occur in a mountainous area probably correspond to flatter terrain than the part covered by deciduous forest. The slope, therefore, will probably be smaller for the grassland than for the forest. This sub-regional variation of terrain results in the spread of points along a given value of  $\alpha_z$ . In Fig. 15, the smaller slopes at  $\alpha_z = 916$  m correspond to cropland and broadleaf forest. The larger slopes occur for evergreen broadleaf and needle and mixed forests. A more highly resolved terrain classification would probably increase the correlation between slope and terrain.

Whether the change in slope with  $\alpha_z$  is due to more shadowing by the mountains or to inadequacies in the BRDFs is not entirely clear. Obviously, the BRDFs for flat lands should not be the same as those for rugged terrain. Thus, some of the correlation in Fig. 15 may be a measure of the errors in the BRDFs. Nevertheless, these initial correlations suggest that the BRDF factors and  $\alpha_z$  can serve as the primary parameters in a model of the BTD angular dependence.

The remaining variance in BTD may be due to VZA-dependent surface emissivity, errors in the atmospheric corrections, parallax and navigation errors, the range of SZA, surface winds, soil moisture, atmospheric humidity, and the vegetation type. Although the limited dataset used here precludes a complete discussion of all of these variables, a few of their effects are briefly mentioned below.

The effects of a VZA-dependent surface emissivity would be most evident for the temperature differences at night over the region having the largest VZA difference. The greatest VZA difference ( $18^\circ$ ) is for region F where  $BTD_9$  averaged only 0.5K at night, a value slightly greater than the uncertainty in the normalizations. This small difference suggests that, for this study, the VZA-dependence of surface emissivity is negligible. Even if it were strongly dependent on VZA, surface emissivity would induce an almost constant offset in BTD with little influence on the diurnal BTD cycles seen here. Similarly, errors in the atmospheric attenuation corrections induce a nearly constant bias between the satellites that will only shift the BTD curves up or down and not affect the range in BTD significantly.

In the above analyses, the G9 and G10 images were adjusted to match the G8 images, but not absolutely registered to a surface map. To estimate the impact of parallax and image registration errors G8 and G9 daytime data taken during April 3, 1998 were selected. All of the G8 images were corrected to match a coastline map projection of the G8 field of view such that apparent movement of the coastlines and other surface features were eliminated in sequences of the images. The corresponding G9 images were then remapped to the GOES-8 projection and compared to the GOES-8 images. Corrections were applied to each G9 image so that the 2 images appeared to be as similar as possible in navigation using the mountainous area of northwestern Mexico as the primary reference instead of the flat land features used in the analyses reported earlier. The results showed very little difference in BTDs when taking into account these 2 problems. For region I forest, the average difference in BTD between the analysis data and this test data was -0.096K with a rms error of 0.102. For flat land data in region A, the mean BTD difference was -0.052K with a rms error of 0.096 K. Thus, the navigation and parallax introduce errors in the BTDs that are less than or equal to 0.1K.



The SZA range will determine the minimum size of the shadowed areas and also the general warming of the atmosphere. Some parts of a scene may never be sunlit so the diurnal cycle in BTM may be even greater in winter than during other seasons. A lower atmosphere with high humidity will tend to warm the surface uniformly by longwave radiation. Thus, humid areas may show smaller BTM ranges for a given  $\theta_z$  and vegetation type than dry areas. Wind will dampen the solar heating of the surface, while soil moisture will inhibit sensible heating by using absorbed sunlight for evaporation.

Vegetation differences appear to have caused some slight differences in BTM for a given region (e.g., Figs. 7 and 8), but these may have been due to slight differences in the topography that are not captured in the terrain dataset. Finer resolution of the terrain both vertically and horizontally will yield greater biases in general (e.g., Lipton and Ward 1997).

One of the limitations of using only GOES data is the restricted angular configuration. For instance, a geostationary satellite cannot see the north side of any scene in the Northern Hemisphere and vice versa for the Southern Hemisphere. Thus, the temperature of the most shaded parts of many scenes cannot be measured and the mean surface temperature for most areas will be overestimated. Furthermore, the minimum radiance at a given time is probably not measured for most regions. McGuire et al. (1988) observed the minimum BTM over a forest canopy around local noon at azimuth angles (relative to north) between  $125^\circ$  and  $225^\circ$  (views toward south-southeast and south-southwest, respectively). Except for regions south of the Tropic of Cancer during the boreal summer, such azimuth angle views are not possible for regions in the Northern Hemisphere from a geostationary satellite. Thus, it is clear that data from other angles are needed to further test the possibility of using topography and BRDFs to account for the variation of  $T_s$  with perspective.

## Concluding Remarks

The results show that land surface brightness temperatures are extremely dependent on the viewing and illumination conditions, topography, and vegetation type. The OLR calculations based on GOES-8 and GOES-9 brightness temperatures measured at the same times show a significant difference. Thus, there will be bias errors if the anisotropy is ignored when using satellite

measurements to derive OLR. Current and future radiation budget measurement systems such as Clouds and Earth's Radiant Energy System on TRMM and the Geostationary Earth Radiation Budget instrument proposed for Meteosat which are limited in their angular coverage of particular regions. To minimize the uncertainty in derived land skin temperatures and OLR from these and other satellites, further quantification of skin brightness temperature anisotropy is needed. It was shown that complex terrain models could reasonably reproduce the radiance fields in rugged terrain. Such models, however, are extremely complex and computer intensive. Simpler models would be required for any operational application. The high correlations between bidirectional reflectance anisotropy and the angular variation of skin temperature and the dependence on terrain variability suggest the potential for a much simpler empirical model. For regions with relatively flat terrain, the vegetation type and soil structure will become more significant and must also be considered in an empirical model.

This study was limited to a few sets of angular pairs. Much more coincident data taken at a variety of angles are needed. A complete set of brightness temperature and reflectance measurements taken at all angles over an entire diurnal cycle for a wide variety of surfaces would constitute the ideal data. In the absence of such datasets, much can be learned from coincident satellite measurements and from further theoretical modeling studies. Measurements of the same area from more than one viewing zenith angle must be used. Combinations of coincident data from geostationary satellites with those in non-geostationary orbits, and from aircraft imagers, should be developed to aid in the pursuit of models to correct for surface longwave emission anisotropy. Corrections for VZA-dependent emissivity and atmospheric attenuation should also be refined. Such research efforts should, in the long run, dramatically reduce the errors in computed and retrieved OLR over land and in the retrieval of surface skin temperatures from satellites.

## **Acknowledgments**

Many thanks to Louis Nguyen, Douglas Spangenberg, and William L. Smith, Jr. of AS&M, Inc. for aiding the data reduction and analysis. David Doelling of AS&M performed the radiative transfer calculations for the flux estimates. David F. Young of NASA Langley Research Center

provided the atmospheric attenuation radiative transfer code. Support for this research was provided by Department of Energy Environmental Sciences Division Interagency Agreement #DE-AI02-97ER62341 as part of the Atmospheric Radiation Measurement Program and by the Earth Observing System Interdisciplinary Program, NASA Earth Sciences Enterprise Office through the Clouds and the Earth's Radiant Energy System Project.

## References

- Benjamin, S.G., J.M. Brown, K.J. Brundage, B.E. Schwartz, T. G. Smirnova, and T. L. Smith, 1994: The operational RUC-2. *Proc. AMS 16th Conf. Weather Anal. and Forecasting*, Phoenix, AZ, 249-252.
- Belward, A. and T. Loveland, 1996: The DIS 1km land cover data set. In *Global Change*, The IGBP Newsletter, #27, Sep., 1996 [Available from IGBP Secretariat, The Royal Swedish Academy of Sciences, Lilla Frescativägen 4, Box 50005, S-104 05 Stockholm, Sweden or via email at sec@igbp.kva.se]
- Fu, Q. and K.-N. Liou, 1993: On the correlated k-distribution method for radiative transfer in nonhomogeneous atmospheres. *J. Atmos. Sci.*, **49**, 2139-2156.
- Kratz, D. P., 1995: The correlated *k*-distribution technique as applied to the AVHRR channels. *J. Quant. Spectrosc. Rad. Transf.*, **53**, 501-507.
- Kriebel, K. T., 1978: Measured spectral bidirectional reflection properties of four vegetated surfaces. *Appl. Opt.*, **17**, 253-259.
- Lagourde, J.P. and Y. Kerr, 1993: Experimental study of angular effects on brightness surface temperature for various types of surfaces. *Proc. of the Workshop on Thermal Remote Sensing of the Energy and Water Balance over Vegetation in Conjunction with Other Sensors*. Sept. 20-23, 1993, La Londe Les Maures, France, 107-111.
- Lipton, A. E. and J. M. Ward, 1997: Satellite-view biases in retrieved surface temperatures in mountain areas. *Remote Sens. Environ.*, **60**, 92-100.

- Masuda, K., T. Takashima, and Y. Takayama, 1988: Emissivity of pure and sea waters for the model sea surface in the infrared window regions. *Remote Sens Environ.*, **24**, 313-329.
- McGuire, M. J., L. K. Balick, J. A. Smith, and R. A. Hutchison, 1988: Modeling directional thermal radiance from a forest canopy. *Remote Sens. Environ.*, **27**, 169-186.
- Minnis, P. and E. F. Harrison, 1984: Diurnal variability of regional cloud and clear-sky radiative parameters derived from GOES data. Part III: November 1978 radiative parameters. *J. Climate Appl. Meteorol.*, **23**, 1032-1052.
- Rossow, W. B. and L. C. Garder, 1993: Cloud detection using satellite measurements of infrared and visible radiances for ISCCP. *J. Climate*, **6**, 2341-2369.
- Sobrino, J. A. and V. Caselles, 1990: Thermal infrared radiance model for interpreting the directional radiometric temperature of a vegetative surface. *Remote Sens. Environ.*, **33**, 193-199.
- Suttles, J. T., R. N. Green, P. Minnis, G. L. Smith, W. F. Staylor, B. A. Wielicki, I. J. Walker, D. F. Young, V. R. Taylor, and L. L. Stowe, 1988: Angular radiation models for Earth-atmosphere system, Vol. 1, Shortwave radiation. *NASA RP-1184*, 144 pp.
- Wong, T., P. Minnis, and C.H. Whitlock, 1996: Anisotropy of surface-emitted radiation. *IRS '96: Current Problems in Atmospheric Radiation*, Aug. 19-24, 1996, Fairbanks, Alaska, 457-460.

## FIGURE CAPTIONS

Fig. 1. Map of study regions showing locations of the relevant satellites.

Fig. 2. Correlation of observed brightness temperatures from (a) G9 and G8 and from (b) G10 and G8 taken at night at 105°W and 90°W, respectively, during April 1998. Regression line fits are also shown.

Fig. 3. Diurnal cycle of apparent skin temperatures for region A grassland from G8 (solid line, triangles), G9 (dashed line, squares), and G10 (dotted, diamonds).

Fig. 4. Skin temperature differences for region A for G8-G9 (dashed, squares) and G8-G10 (dotted, diamonds). Local sunrise (SR), noon (N), and sunset (SS) are indicated with the heavy tick marks.

Fig. 5a. Same as Fig. 4, except for G8-G10 over region B open shrubland (dashed, squares), grassland (dotted, diamonds), and evergreen needle forest (solid, triangles).

Fig. 5b. Same as Fig. 5a, except for G8-G9.

Fig. 6. BTD for region C water surface corrected for emissivity for G8-G9 (dashed, squares) and G8-G10 (dotted, diamonds) and uncorrected for emissivity for G8-G9 (dashed) and G8-G10 (dotted).

Fig. 7a. Diurnal cycle of apparent skin temperatures for region D forest from G8 (solid line, triangles), G9 (dashed line, squares), and G10 (dotted, diamonds).

Fig. 7b. Same as Fig. 5a, except for region D open shrubland (dashed, squares), crop/grassland (dotted, diamonds), and combined forest (solid, triangles).

Fig. 7c. Same as Fig. 5b, except for region D open shrubland (dashed, squares), grassland (dotted, diamonds), and deciduous forest (solid, triangles).

Fig. 8a. Same as Fig. 5a, except for region E crop/grassland (dotted, diamonds) and evergreen needle forest (solid, triangles).

Fig. 8b. Same as Fig. 5b, except for region E cropland (dotted, diamonds) and evergreen needle forest (solid, triangles).

Fig. 9. Skin temperature differences for region F crop/mosaic for G8-G9 (dashed, squares) and G8-G10 (dotted, diamonds).

Fig. 10. Skin temperature differences between G8 and G9 for crop/grassland in region G (dotted, diamonds) and combined forest for region H (solid, triangles) during May 1998. Local sunrise (SR), noon (N), and sunset (SS) are indicated with the heavy tick marks.

Fig. 11a. Same as Fig. 5a, except for region I combined forest (solid, triangles), and crop-mosaic (dotted, diamonds).

Fig. 11b. Same as Fig. 5b, except for region I combined forest (solid, triangles), and crop-mosaic (dotted, diamonds).

Fig. 12. Difference in OLR computed using G8 and G9 surface temperatures for region A grassland (dotted, diamonds), region B grassland (dashed, squares), and region I deciduous broadleaf forest (solid, triangles).

Fig. 13. Time series of skin temperature differences between GOES-8 and 9 for region B evergreen forest area (dotted, diamonds) and GOES-8 (solid, triangles) and GOES-9 BRDF factors (dashed, squares).

Fig. 14. Correlation between  $BTD_9$  and the difference in BRDF factors for G8 and G9 for region A grassland (dotted, diamonds), region B evergreen forest (solid, triangles), and region I evergreen forest (dashed, squares) for days 93 and 94, 1998.

Fig. 15. Variation of slope in (5) for  $BTD_9$  (dashed, squares) and  $BTD_{10}$  (dotted, diamonds) for all of study regions as a function of  $z$ .

Table 1. Characteristics of study regions and viewing angles from GOES. Only major vegetation types are noted for each region.

Region	Latitude (°N), Longitude (°W)	IGBP Types (% coverage)	Z (m)	$z$ (m)	G8 VZA (°)	G9 VZA (°)	G10 VZA (°)
A	33.5, 103.5	Grass (100)	884	125	49.5	51.5	39.0
B	34, 106	Evergreen forest (13) Open Shrub (56) Grass (31)	1419	413	51.5	50.2	39.5
C	27.5, 111.5	Water (100)	0	0	51.3	41.3	32.9
D	30, 112	Open shrub (28) Deciduous forest (35) Evergreen Forest (15) Grass (9)	341	241	53.2	43.1	35.8
E	31, 95	Evergreen forest (63) Crops (30)	39	14	42.4	56.2	37.7
F	35, 91	Deciduous forest (8) Woody savanna (11) Crops/Mosaic (67) Urban (1)	48	24	44.1	61.5	43.3
G	51.5, 111.5	Evergreen forest (19) Mixed forest (81)	753	32	68.0	62.9	59.2
H	57.5, 115.5	Grass (19) Crops/Mosaic (70)	583	88	74.2	67.6	66.0
I	26, 108	Evergreen forest (33) Deciduous forest (27) Mixed forest (21) Crops/Mosaic (12)	1050	916	47.5	42.7	30.6
J	30, 110	Deciduous forest (46) Mixed forest (45)	1388	591	51.6	44.4	35.4
K	28, 110	Deciduous forest (47) Mixed forest (26)	560	601	50.4	42.7	33.1
L	32, 108	Open shrub (86) Grass (13)	1280	161	51.5	47.3	37.4
M	30, 108	Evergreen forest (44) Open shrub (10) Grass (38)	1824	470	50.1	45.7	35.1

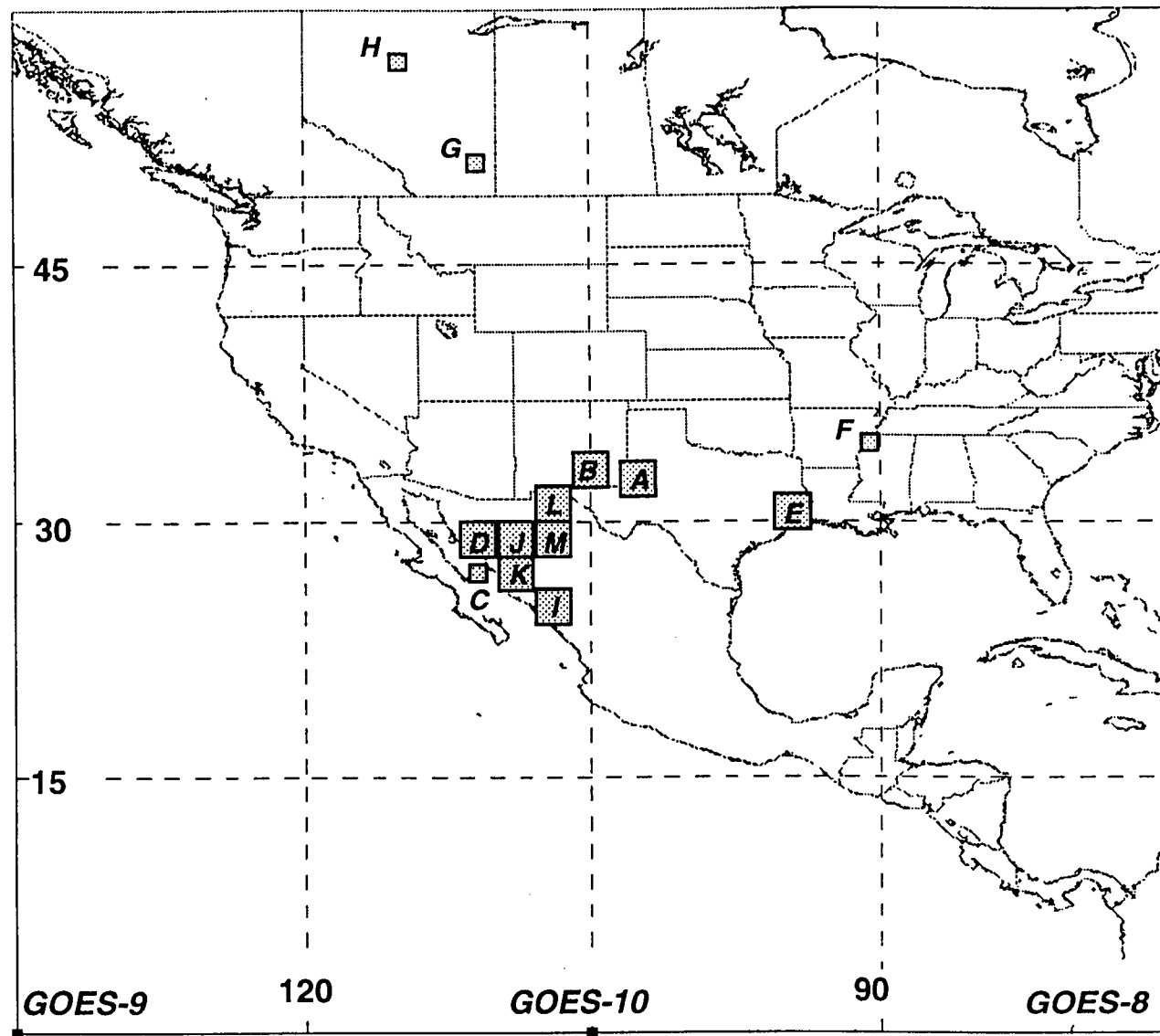


Fig. 1.



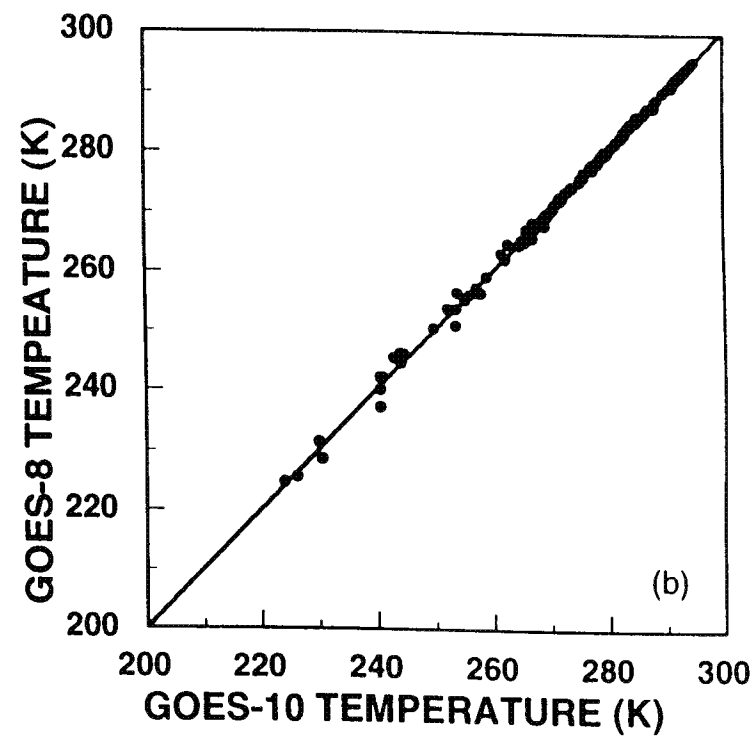
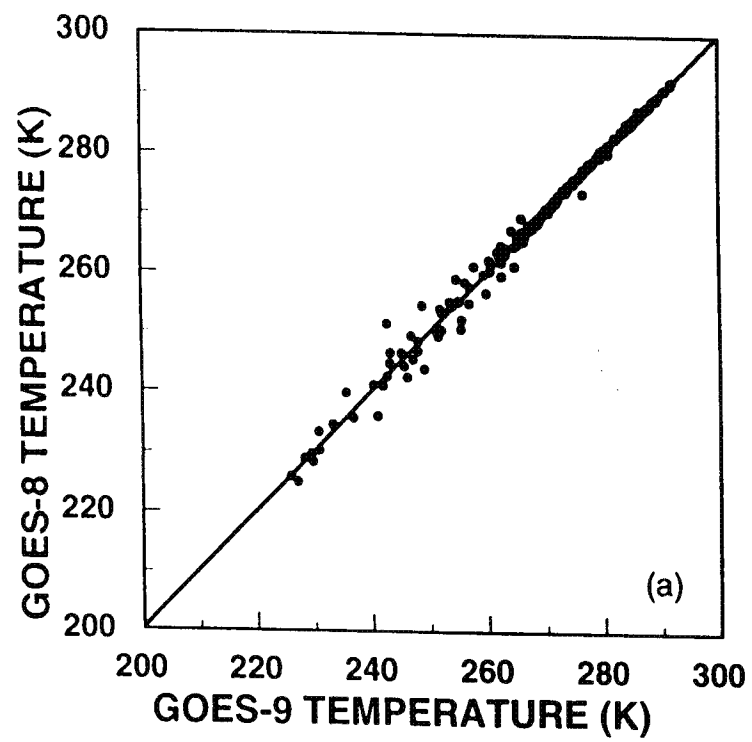


Fig. 2.

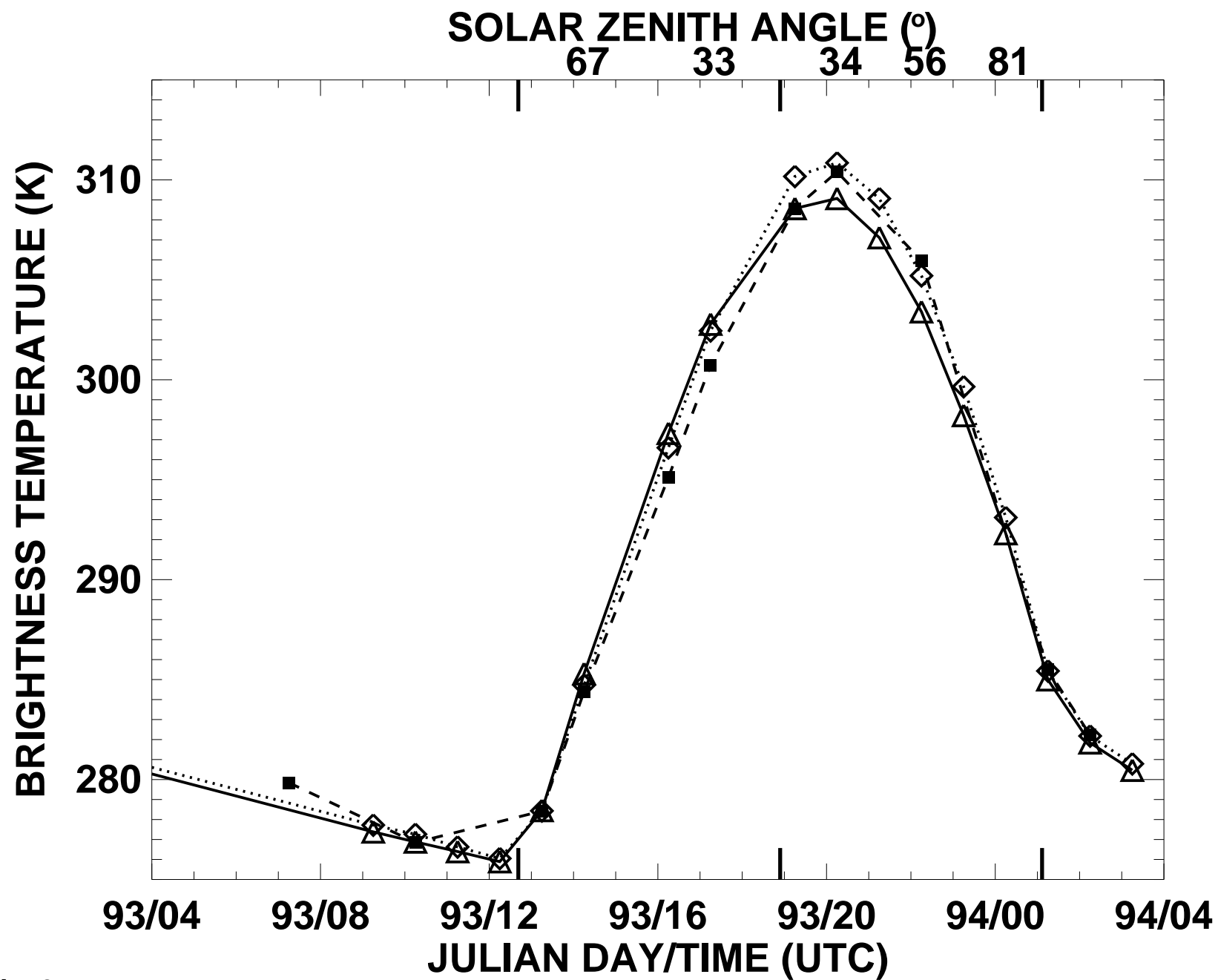


Fig. 3

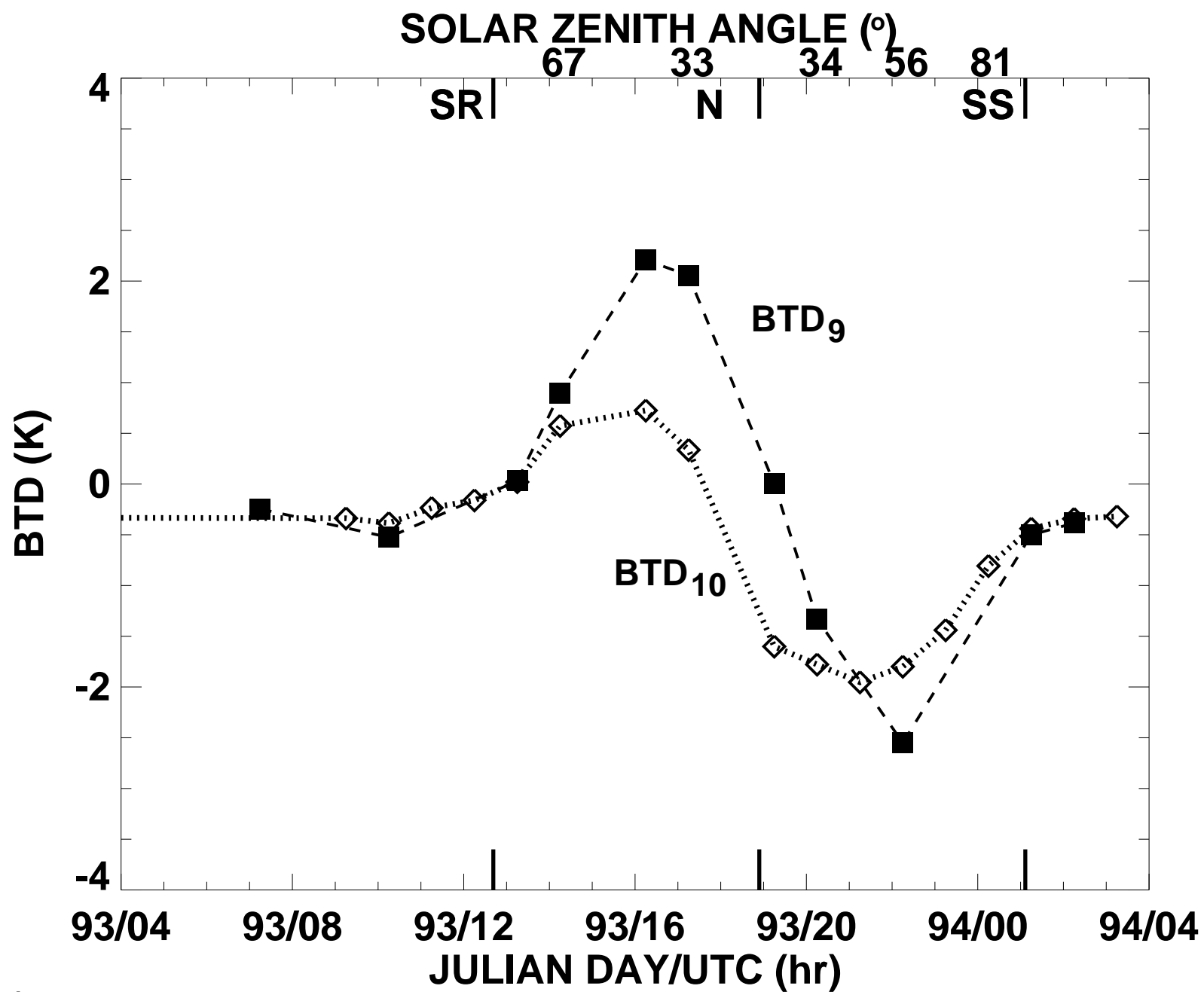


Fig. 4

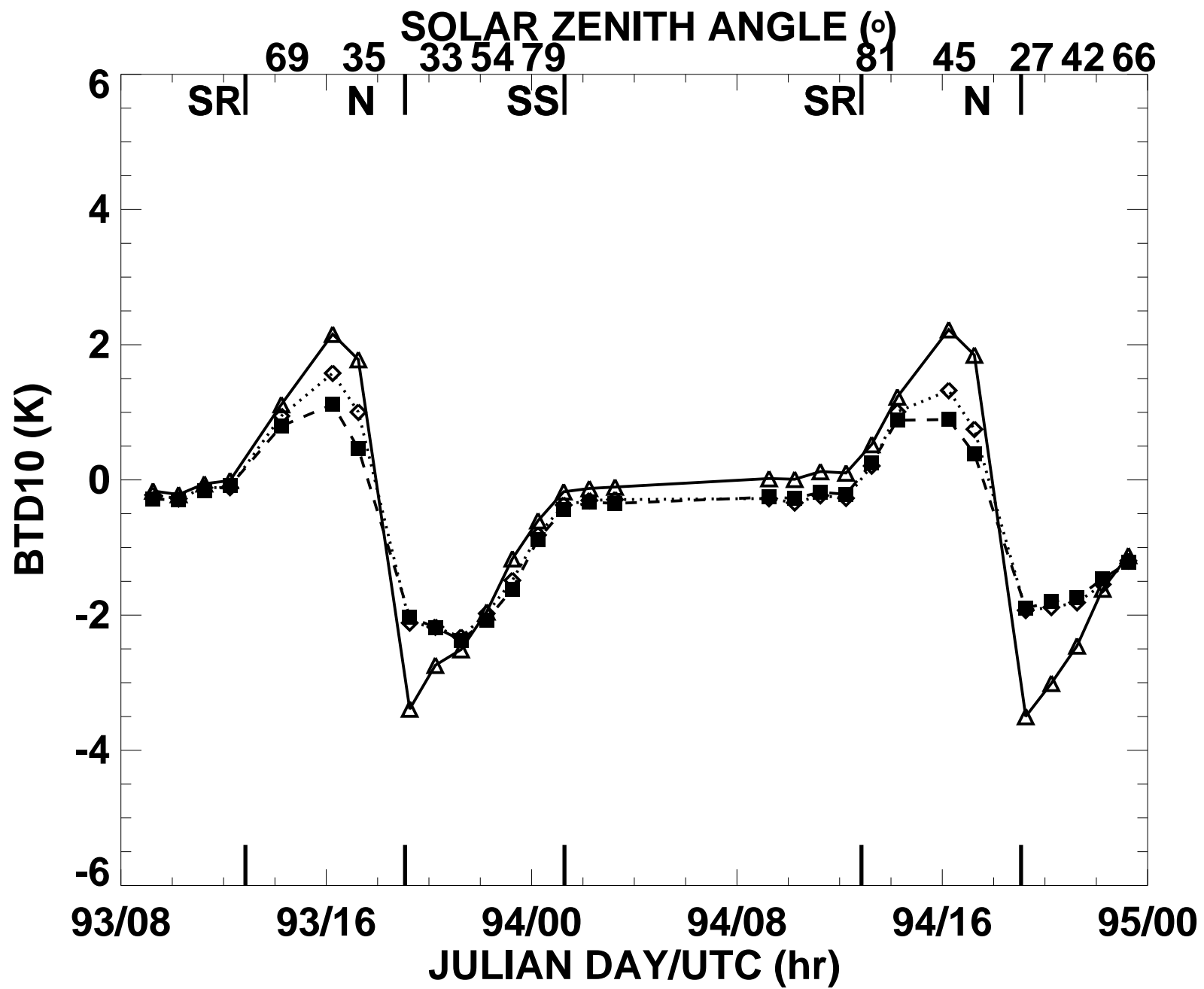


Fig. 5a

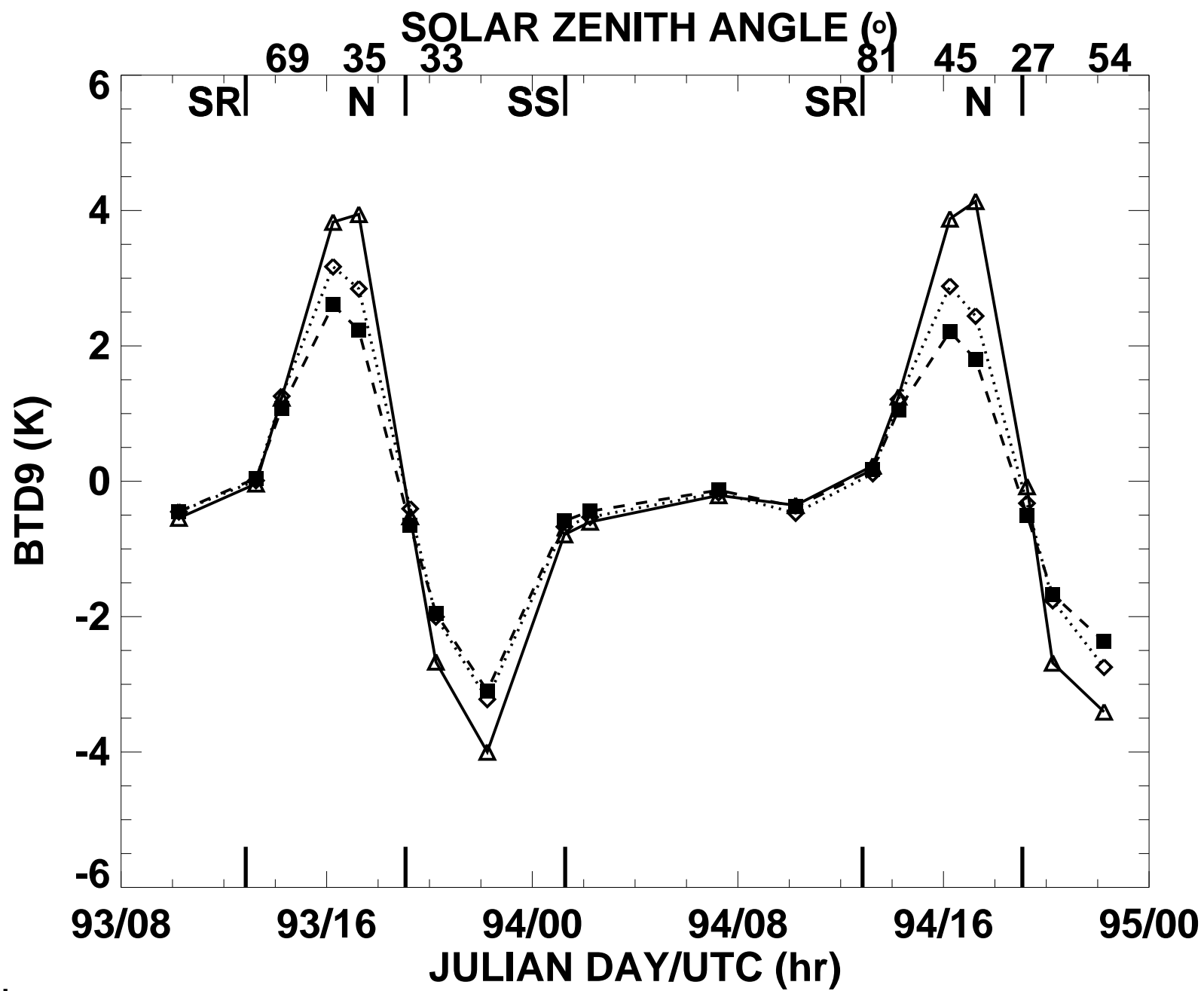


Fig. 5b

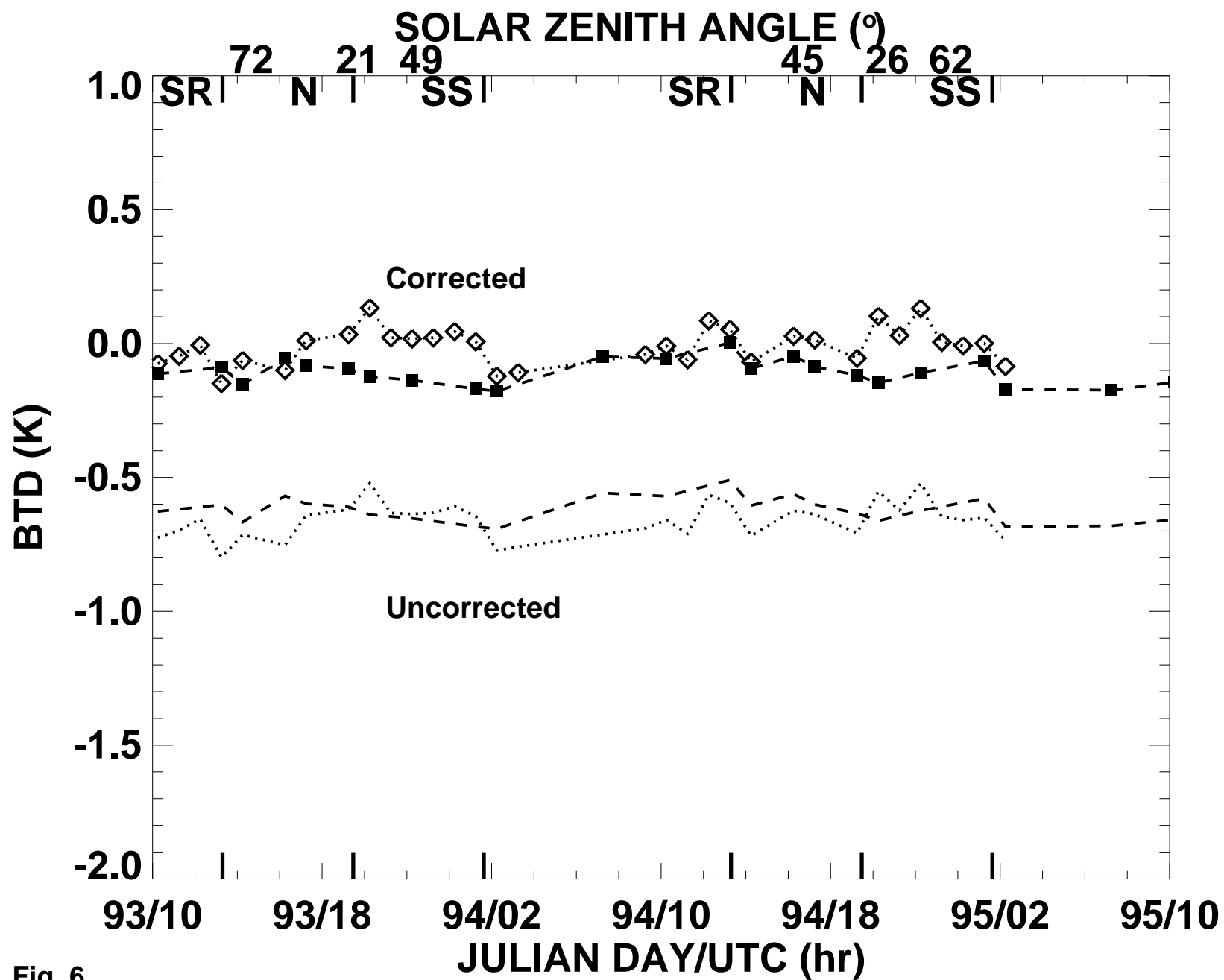


Fig. 6

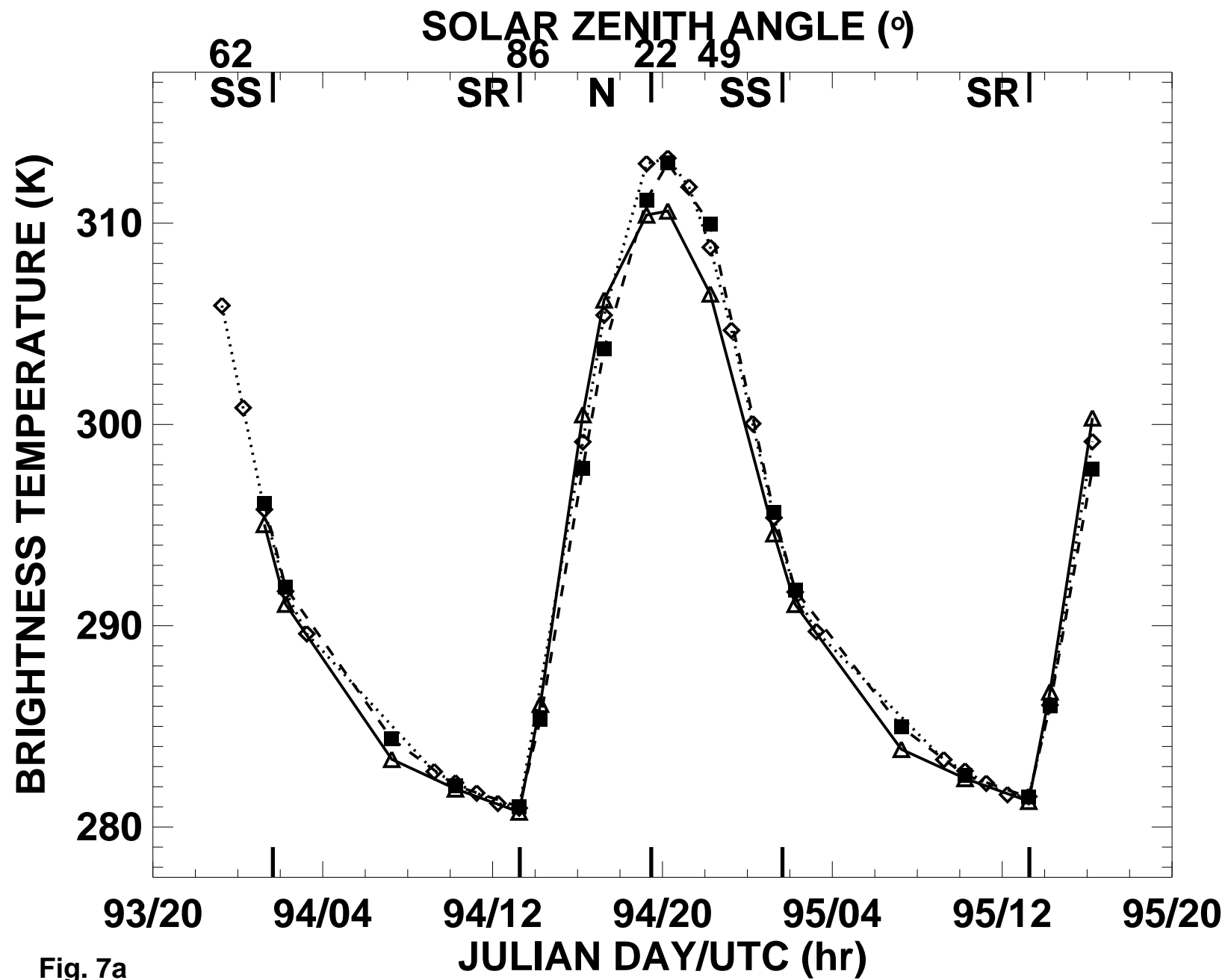


Fig. 7a

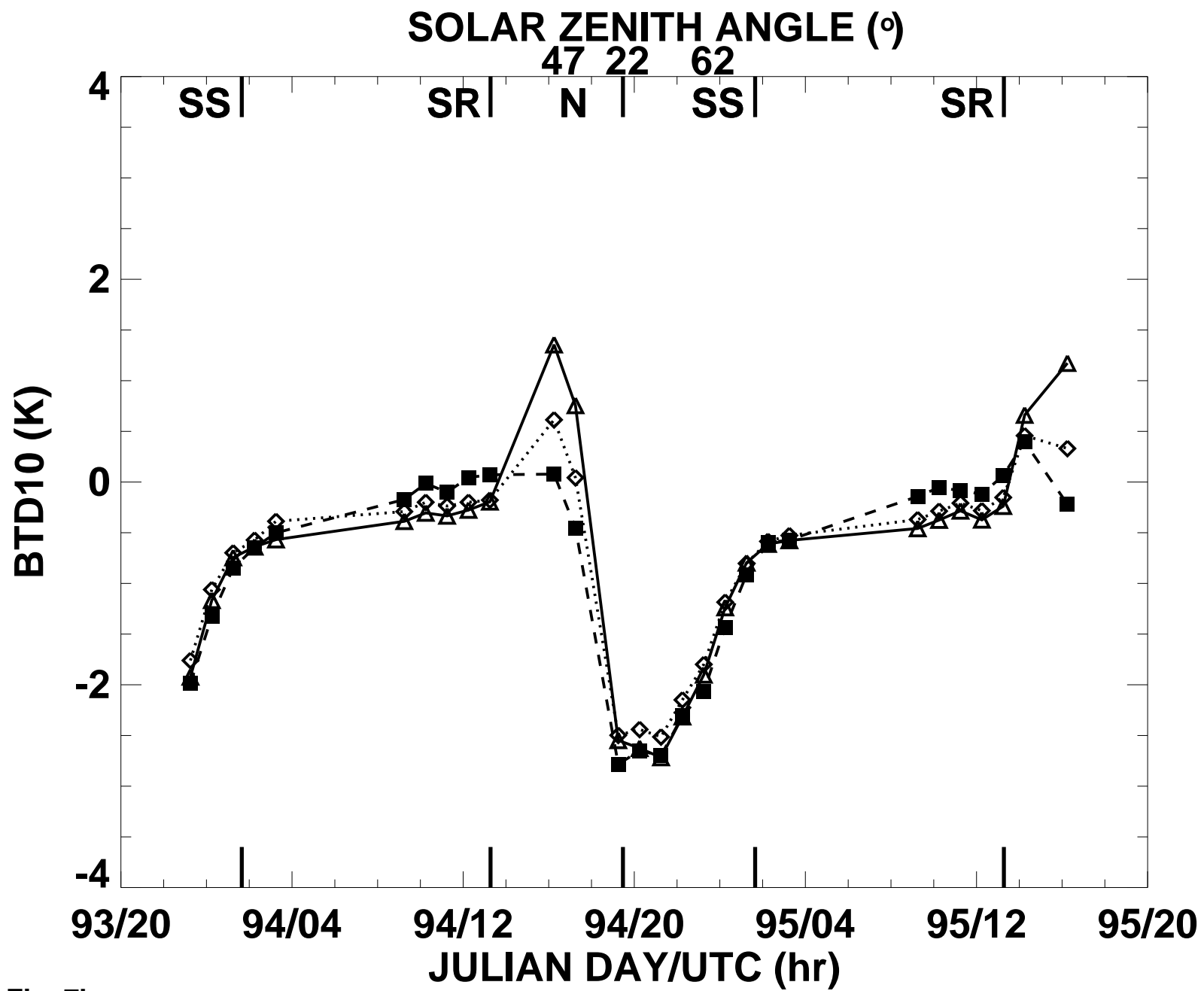


Fig. 7b



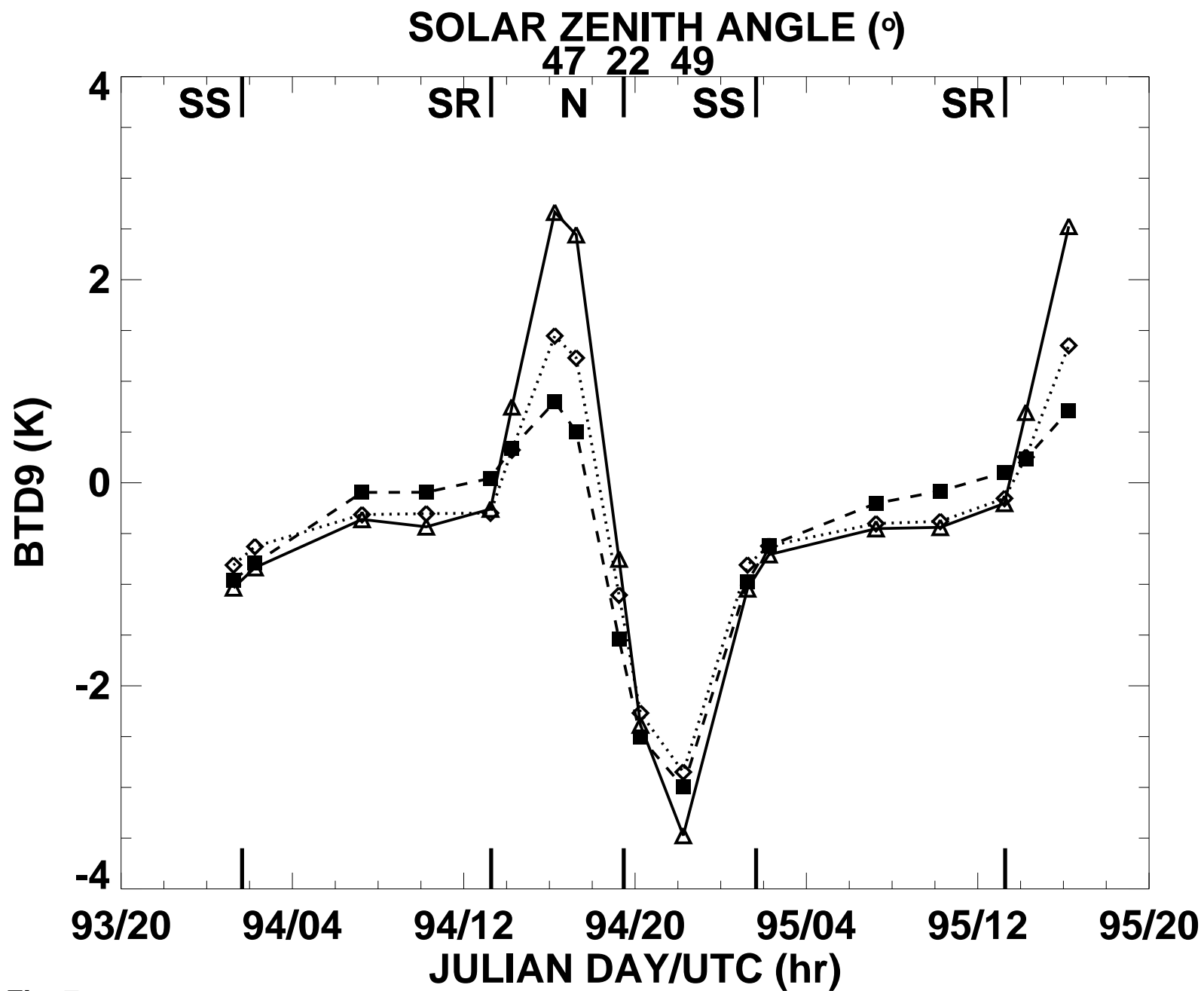


Fig. 7c

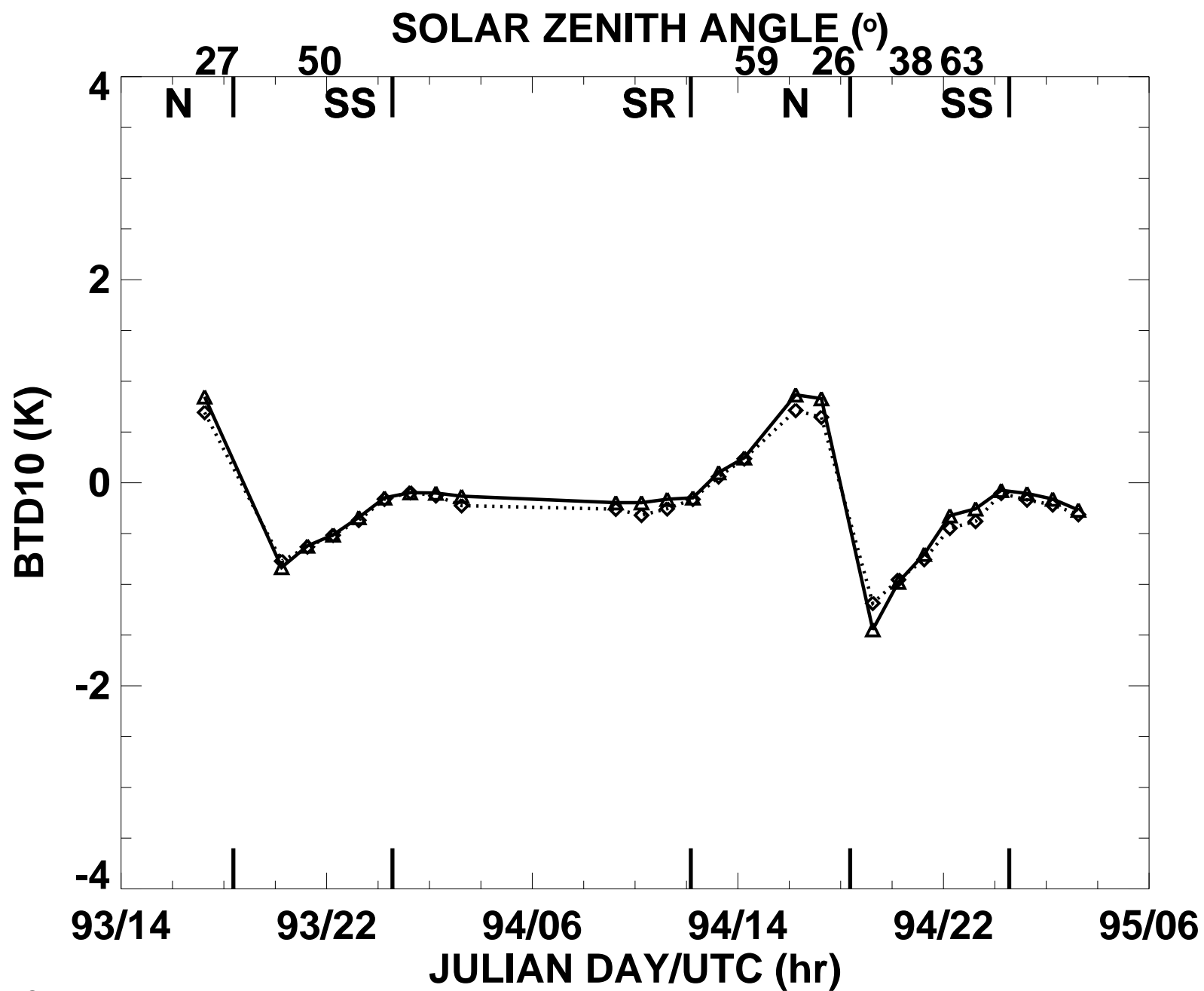


Fig. 8a

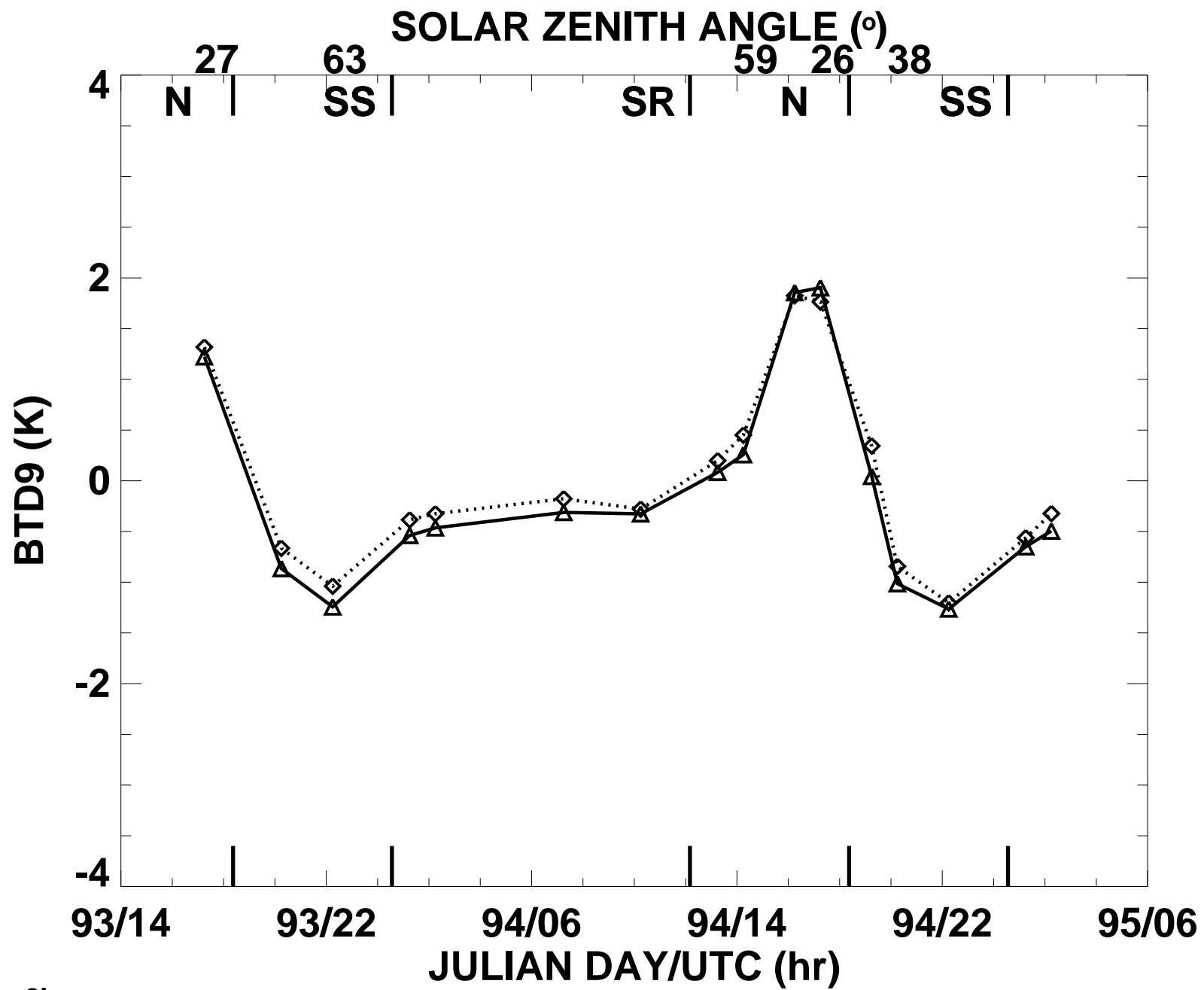


Fig. 8b

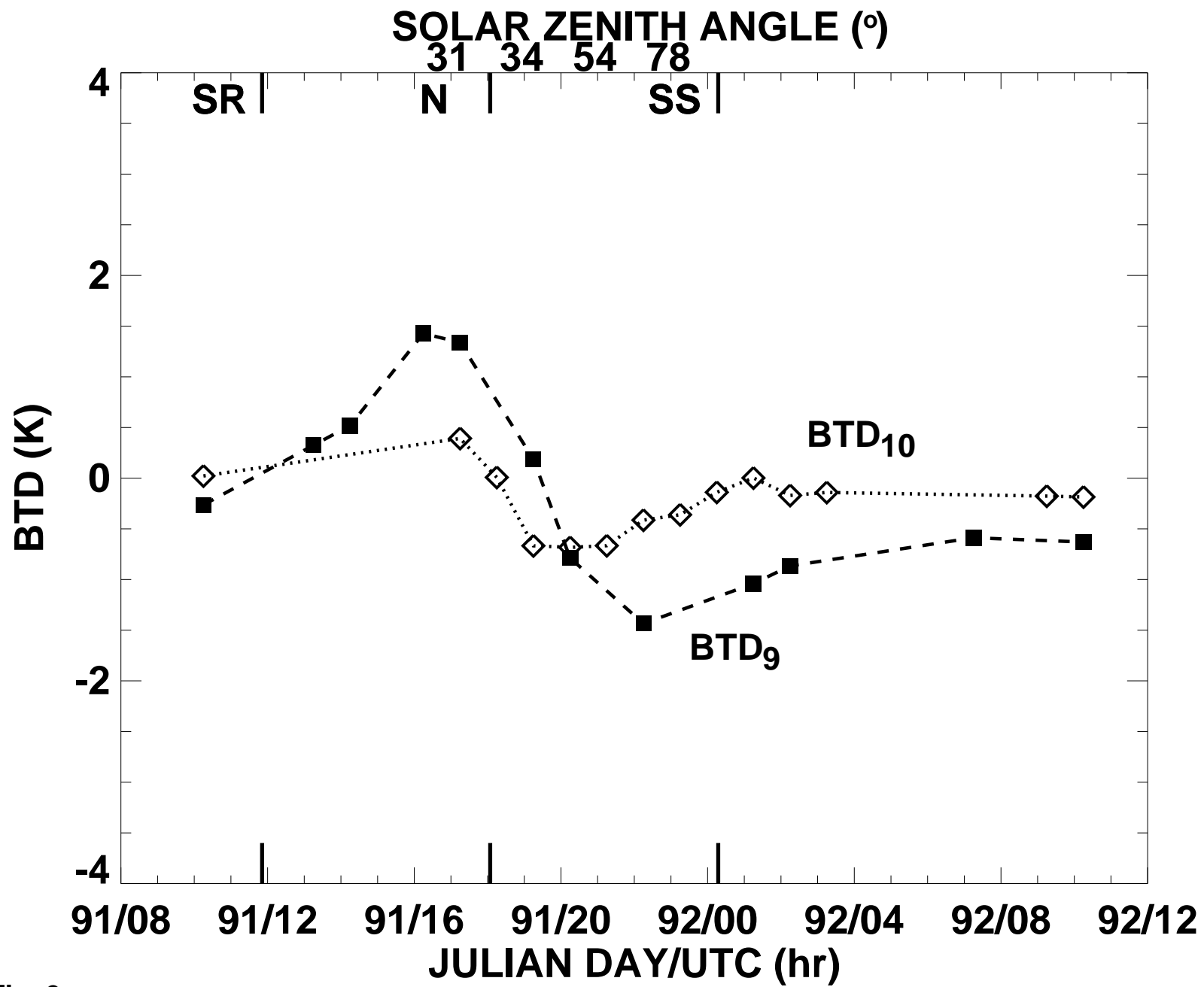


Fig. 9

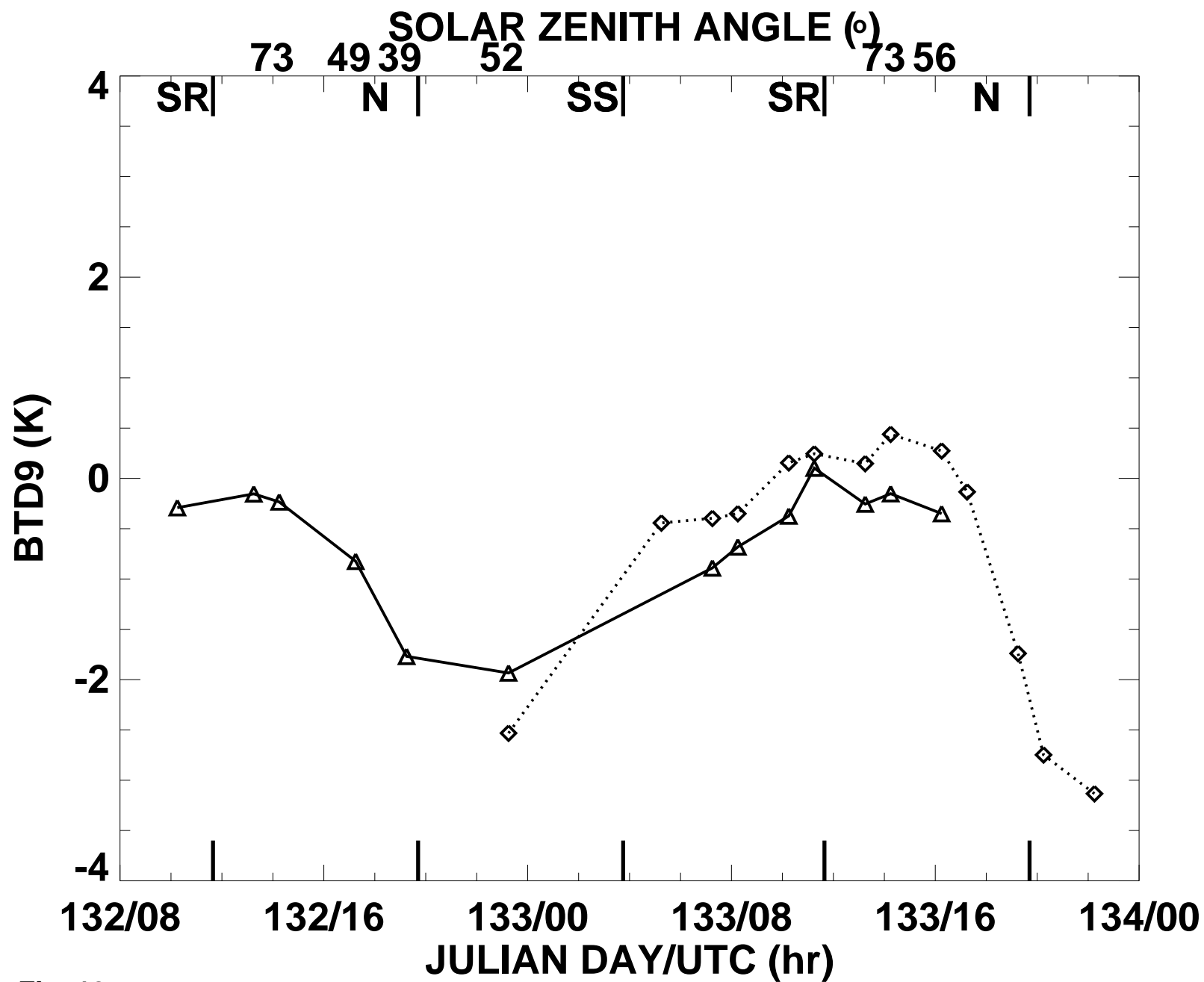


Fig. 10

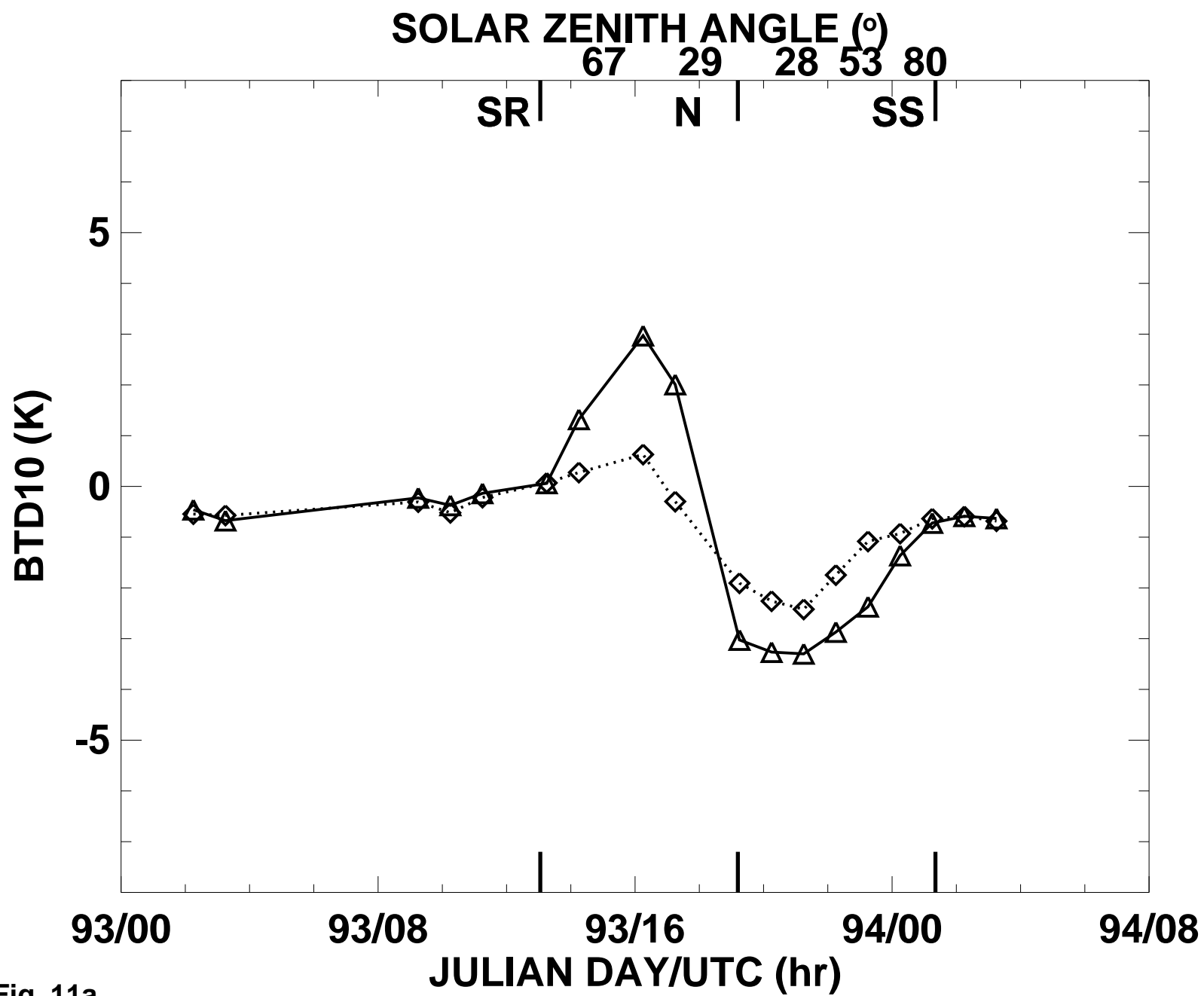


Fig. 11a

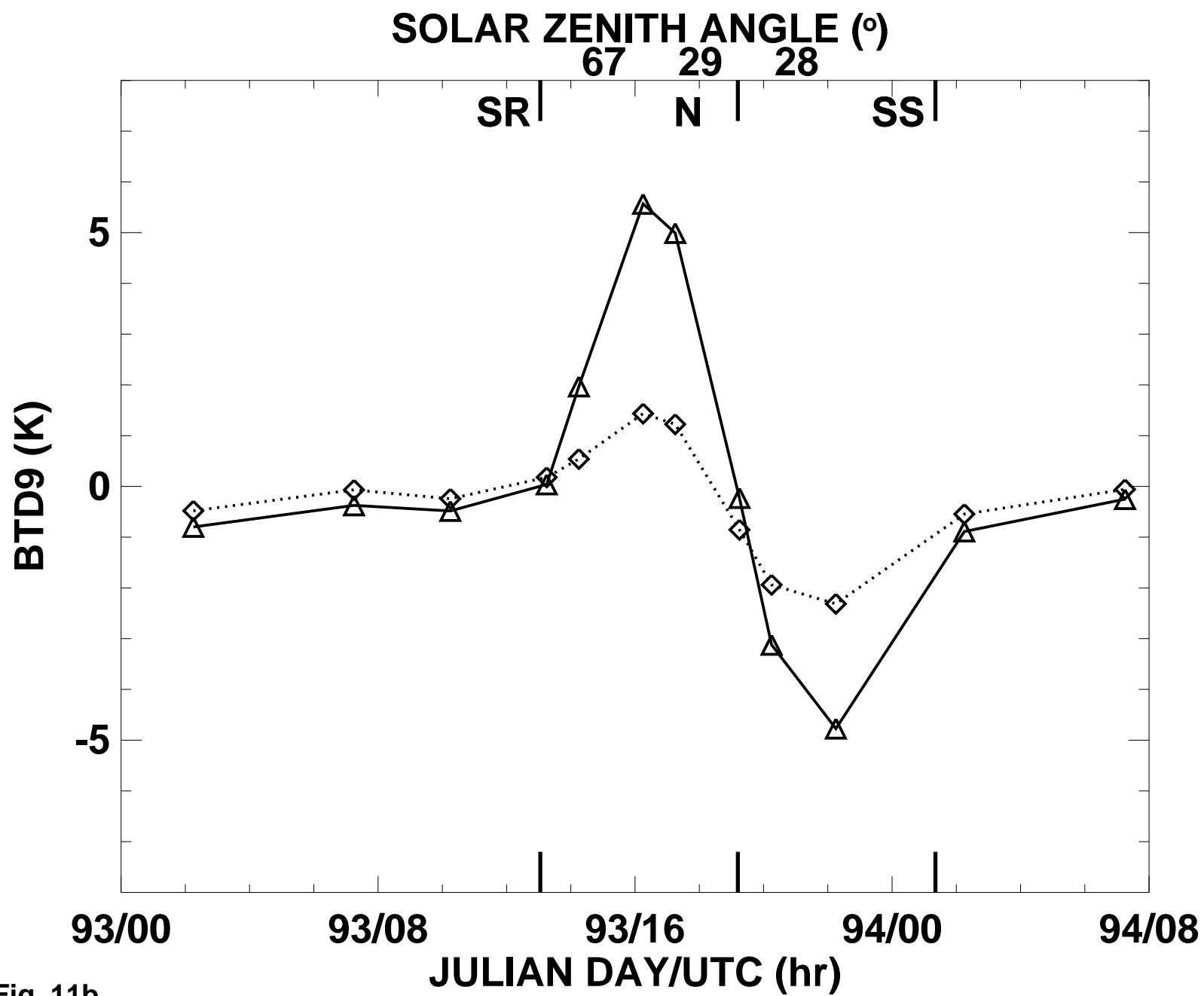


Fig. 11b

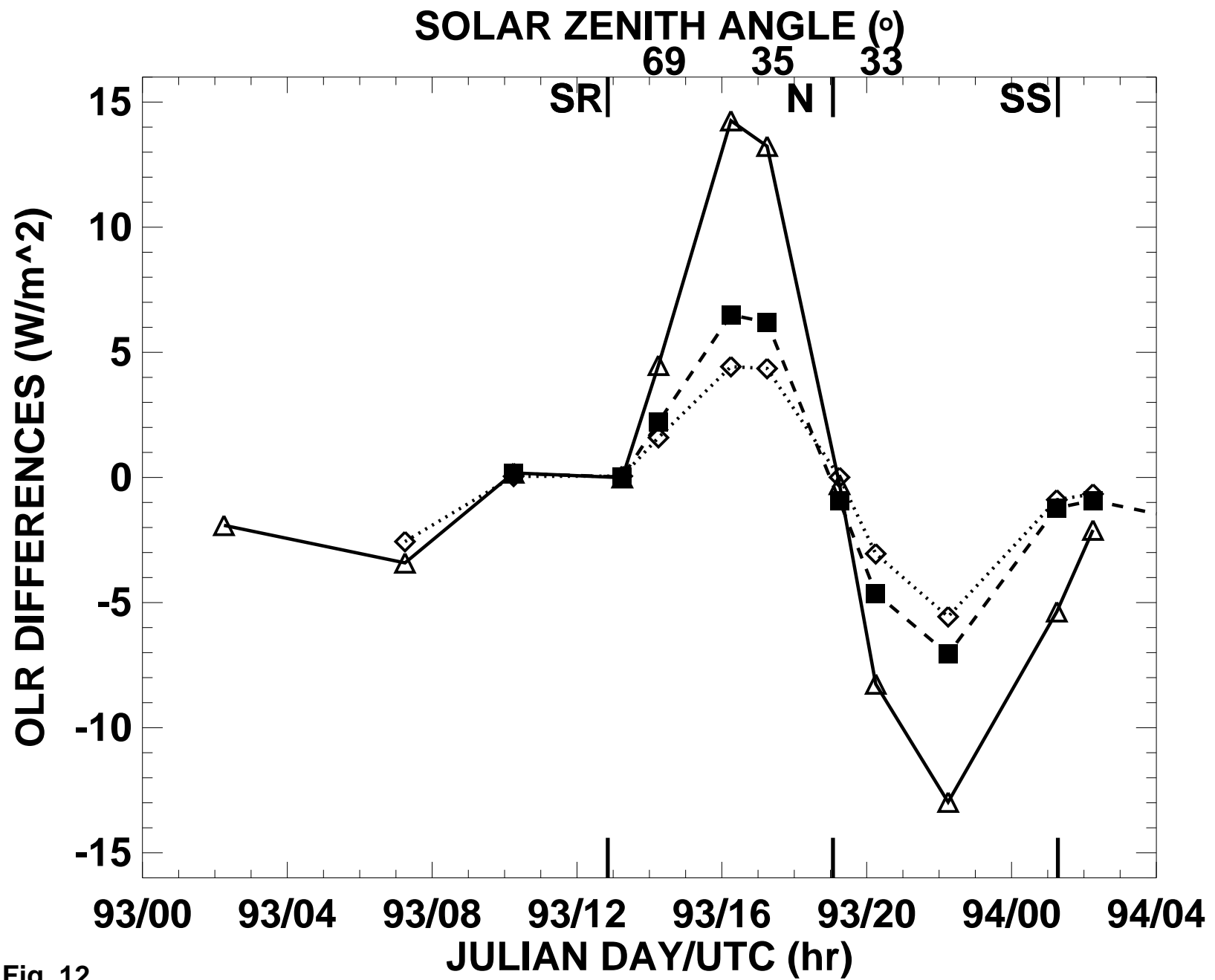


Fig. 12



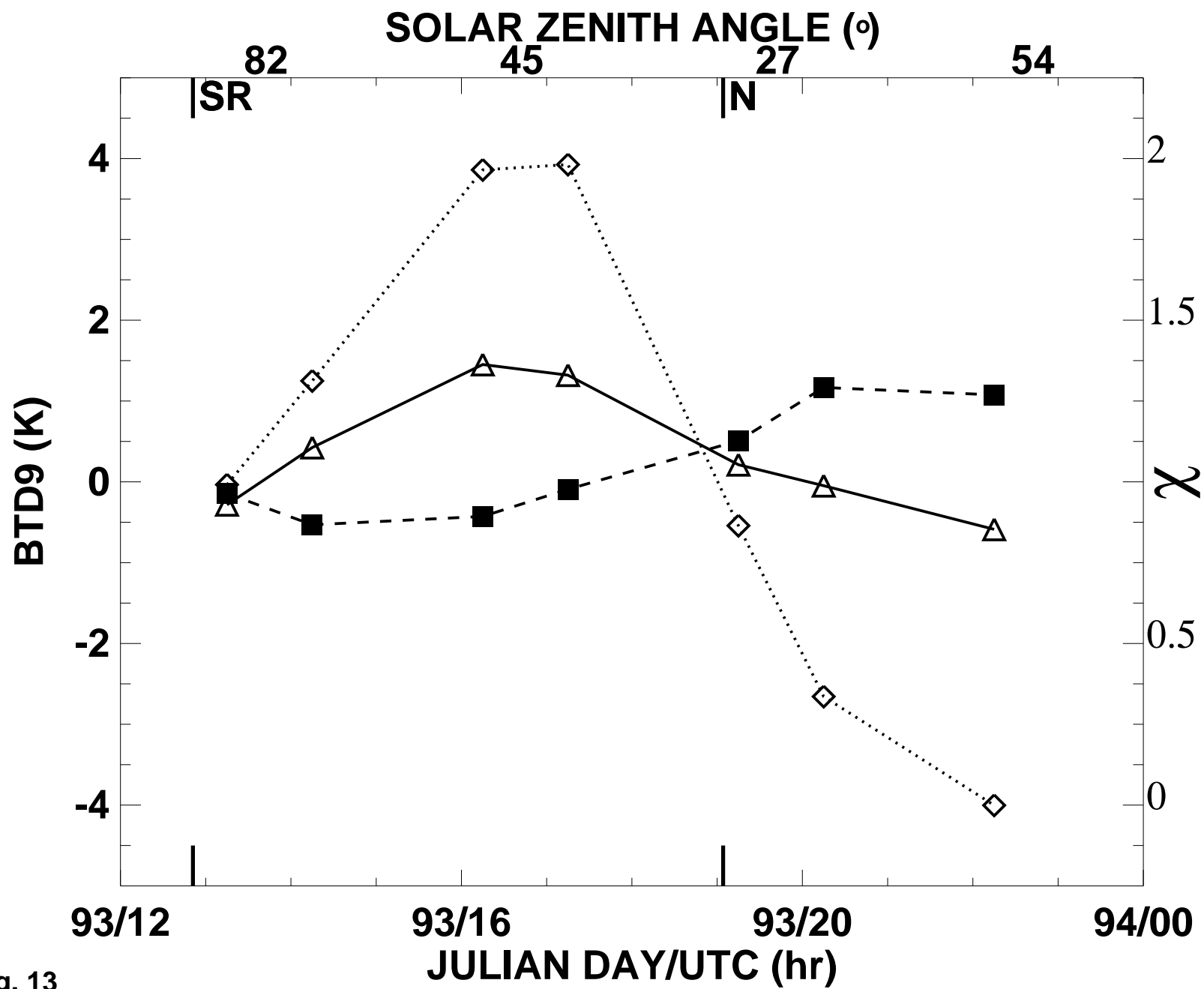


Fig. 13

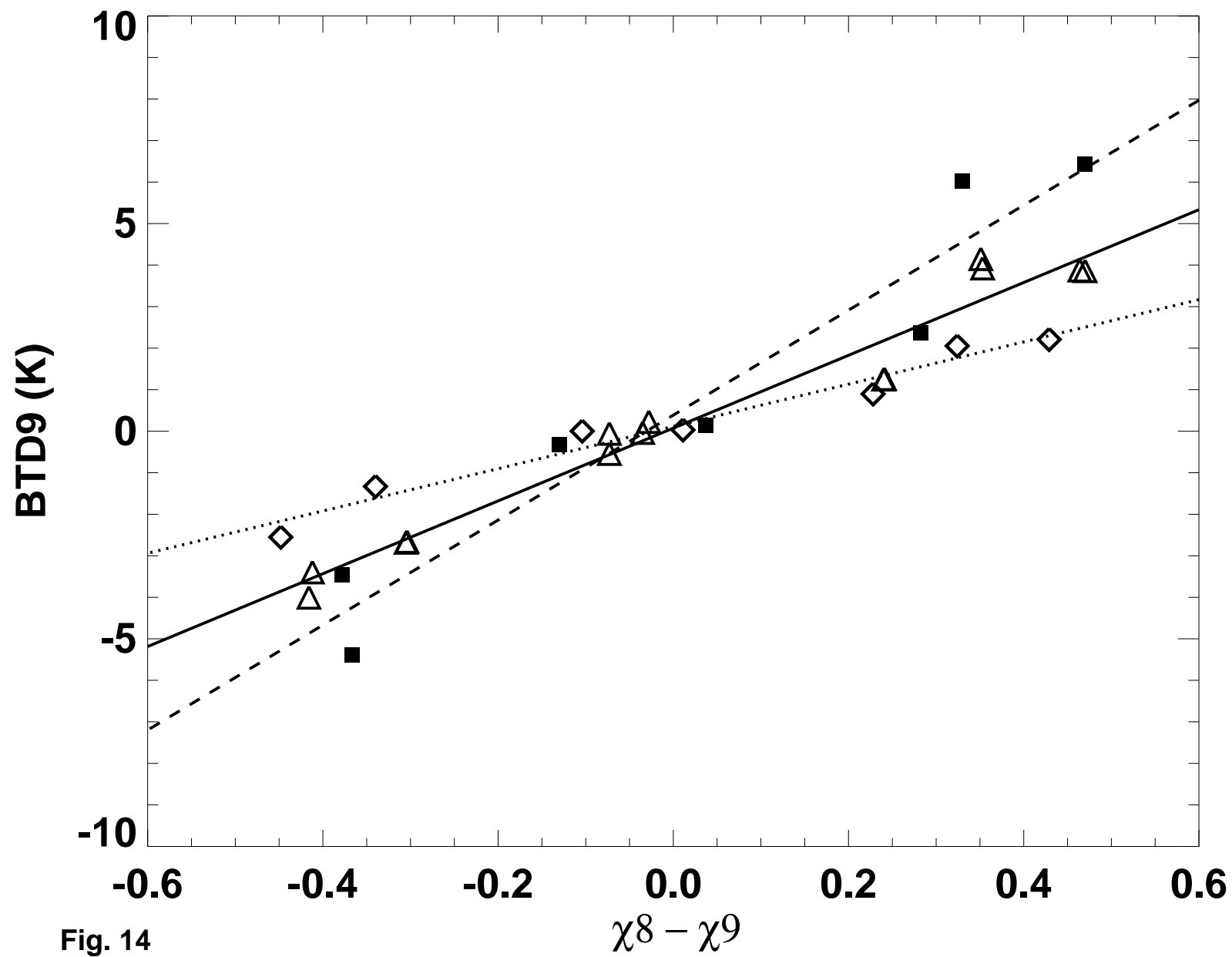


Fig. 14

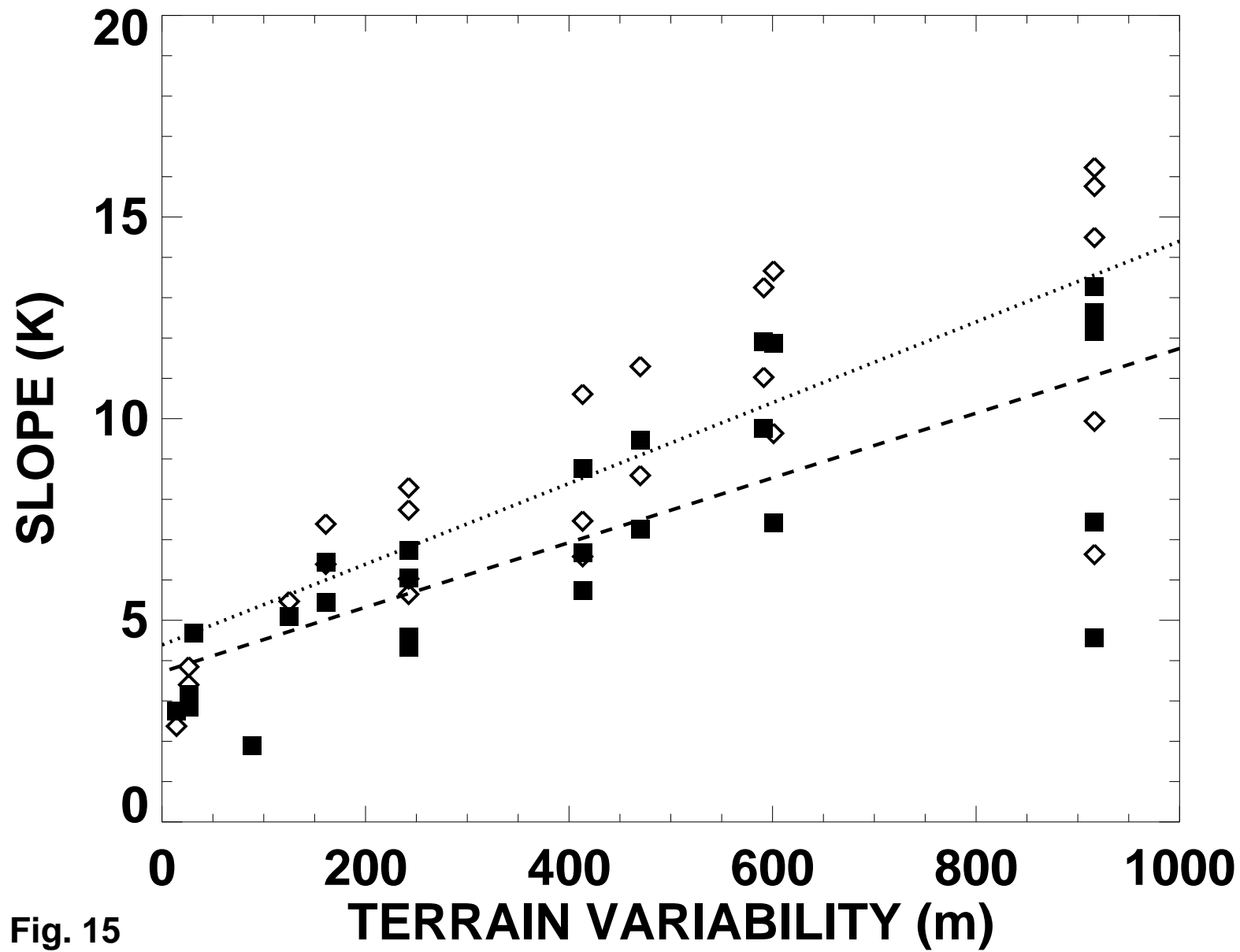


Fig. 15